Materials Advances

ROYAL SOCIETY OF CHEMISTRY

REVIEW

View Article Online
View Journal | View Issue

Cite this: *Mater. Adv.*, 2023, 4, 389

A focused review on structures and ionic conduction mechanisms in inorganic solid-state proton and hydride anion conductors

Shichen Sun, Qiming Tang, Kangkang Zhang, Yeting Wen, Aidan Billings and Kevin Huang *

Solid-state proton and hydride anion conductors are an important family of materials as electrolytes for solid state electrochemical cells such as fuel cells, batteries, sensors, and gas separation membranes. Searching for new proton and hydride-anion conductors has been an active research area for many decades. The focus of this article is on reviewing the types and mechanisms of each proton/hydride-anion conductor developed and their pros and cons. This review starts off with the most studied and most promising perovskite structured oxides as proton conductors, followed by other types of perovskite-related structures such as the Ruddlesden–Popper phase, pyrochlores and rare earth ortho-niobates/orthotantalates. This review then moves to solid polyanionic compounds as proton conductors, including sulfates, nitrates, and phosphates, which is followed by hydrates and nanocomposites. This review finally discusses the types and conduction mechanisms of new hydride-anion conductors that emerged recently.

Received 27th October 2022,
Accepted 21st November 2022

DOI: 10.1039/d2ma01003h

rsc.li/materials-advances

1. Introduction

Many solids exhibiting fast proton (H^+) and hydride ion (H^-) conduction have been reported for decades. It is generally understandable that H^+ and H^- move fast in solids due to their size and charge.[1] Like any ionic conductors, H^+/H^- conductors can be used as an electrolyte in electrochemical cells for H_2 conversion and storage; the latter is a vital clean technology to combat climate crisis and build a carbon pollution-free economy. In general, H^+/H^- conductors are found in both organic and inorganic materials. Organic materials, such as Nafion (perfluorosulfonic acid polymer), show high proton conductivity at low temperatures (<90 °C) under hydrated conditions, while inorganic materials, on the other hand, show H^+/H^- conduction in a higher and wider temperature range. In this review, we will focus primarily on the inorganic H^+/H^- conductors. Despite many existing reviews on H^+ conducting materials in the literature, they are mostly focused on material properties and applications in energy conversion and storage.[2–5] A review encompassing both H^+/H^- conductors with a focus on structure and ionic conduction mechanisms is still lacking. In this article, we aim to fill this gap by reviewing recent progress of inorganic solid-state fast H^+/H^- conductors in the perspectives of synthesis, structure and phase transformations, conductivity, and conduction mechanisms.

The inorganic proton conductors reviewed in this article include solid oxides, solid polyanionic salts, and hydrates. The solid-oxide family includes perovskites, Ruddlesden–Popper intergrowths, and *ortho*-niobates/*ortho*-tantalates; the solid polyanionic salt family includes inorganic acids, sulphates, and phosphates/pyrophosphates; the hydrate family includes hygroscopic mesoporous materials. Compared to the well-studied proton conductors, hydride anion (H^-) conductors are under studied. Although H^- has a larger size than H^+, it is still small enough for fast ion transport and is a strong reducing agent that could find unique applications in energy storage and conversion devices. For these reasons, there has been growing interest in H^- conductors in recent years. This class of materials includes hydrides, nitride-hydrides, perovskite oxyhydrides, and hydroflurides. In the following, we review the key aspects of these H^+/H^- conductors.

2. Solid oxide proton conductors

2.1 Perovskite oxides

One of the most studied proton conductors is perovskite oxides. The typical chemical formula of the perovskite oxides is ABO_3, where A and B denote two different cations, see Fig. 1. A typical

Department of Mechanical Engineering, University of South Carolina, Columbia, SC29201, USA. E-mail: huang46@cec.sc.edu

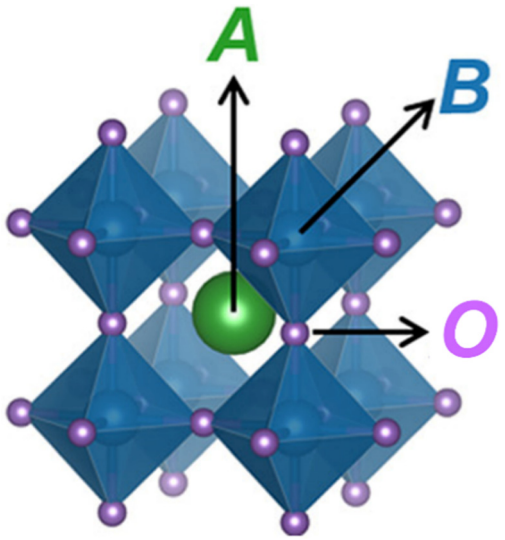

Fig. 1 The ideal structure of ABO_3.[13]

ABO_3 structure consists of a large 12-coordinated A cation (A = Ca, Sr, Ba, La, and Gd), and a small 6-coordinated B cation (B = Nb, W, Ce, Zr, Ti, Mn, Fe, Co, and Ga). The ideal ABO_3 structure is primitive cubic, but many ABO_3 exhibit a lower symmetry (*e.g.*, hexagonal and orthorhombic) with slightly distorted unit cells because of the ionic size effect as described by the Goldschmidt's tolerance factor. Based on the types of A and B cations, ABO_3 can be an ionic conductor, semiconductor, and electronic conductor, finding applications in electrochemical devices such as solid oxide fuel cells and catalytic membrane reactors.[6–12]

For a perovskite oxide to be a proton conductor, a proton in the form of $OH_O^{\bullet}$ on the O^{2-}-sub-lattice can be generated by a hydration process under humid conditions or a hydrogenation process under reducing conditions as illustrated by the following Kröger–Vink defect reactions:

$$H_2O + V_O^{\bullet\bullet} + O_O^{\times} \leftrightarrow 2OH_O^{\bullet} \quad (1)$$

$$H_2 + 2O_O^{\times} \leftrightarrow 2OH_O^{\bullet} + 2e' \quad (2)$$

Clearly, the concentration of OH^- is favored by higher partial pressure of H_2O (pH_2O), oxygen vacancy ($V_O^{\bullet\bullet}$) concentration, and lattice oxygen ($O_O^{\times}$) concentration. Since the reactions are exothermic, *e.g.*, the enthalpy (ΔH°) of the reaction (1) for $BaCe_{0.9}Y_{0.1}O_{3-\delta}$ and $BaZr_{0.8}Y_{0.2}O_{3-\delta}$ are −163.3 and −79.5 kJ mol^{-1}, respectively,[4] the proton concentration ($OH_O^{\bullet}$) decreases with temperature.[3,14,15]

Two proton conducting mechanisms have been proposed to describe the H^+ transport in the perovskite-type oxides:[15,16] (1) the Grotthuss mechanism, Fig. 2(a), where H^+ migrates *via* reorientation of H^+ and the formation and cleavage of H-bonds with the adjacent lattice O, and (2) the vehicle mechanism, Fig. 2(b), in which H^+ is first bonded with O^{2-} to form OH^- (or ($OH_O^{\bullet}$) by Kröger–Vink notations) and then diffuses through $V_O^{\bullet\bullet}$. There has been increasing evidence in recent years showing that both Grotthuss and vehicular mechanisms are involved in the H^+ transport in perovskite oxides.

Due to the presence of $V_O^{\bullet\bullet}$, perovskite proton conductors can also be good oxide-ion conductors, depending on the conditions. For example, H^+ conductivity dominates under high pH_2O, low pO_2, and low temperature, whereas O^{2-} conductivity is favored by dry and high temperatures.[18] The magnitude of proton conductivity also depends on the material composition. For example, Ba-containing perovskites such as $BaCeO_3$ and $BaZrO_3$ are among the best in all proton conductors studied so far.

The first reported perovskite H^+ conductor was doped $SrCeO_3$.[19,20] Since then, doped $BaZrO_3$ and $BaCeO_3$ have become the most studied proton conductors due to their higher conductivity.[10,21–26] In general, doped $BaCeO_3$ exhibit a higher conductivity (*e.g.* $\sim 2 \times 10^{-2}$ S cm^{-1} at 600 °C) than doped $BaZrO_3$,[27,28] but their chemical stability in H_2O and CO_2 is generally poorer. To achieve a good balance among chemical stability, ionic conductivity, and mechanical property, "solid solution" mixing between $BaCeO_3$ and $BaZrO_3$ is a widely adopted strategy. However, to further increase the degree of

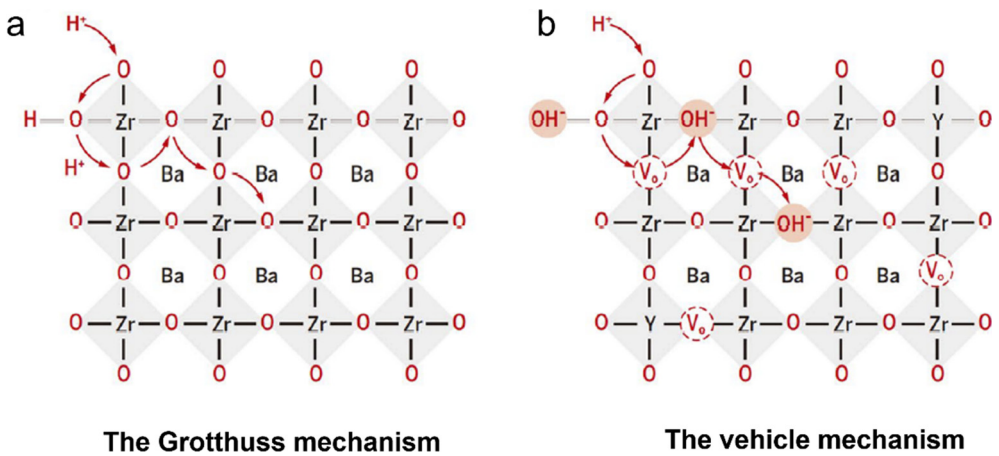

Fig. 2 Schematics of two H^+ conducting mechanisms in a $BaZrO_3$-based perovskite oxide: (a) the Grotthuss mechanism and (b) the vehicle mechanism.[17]

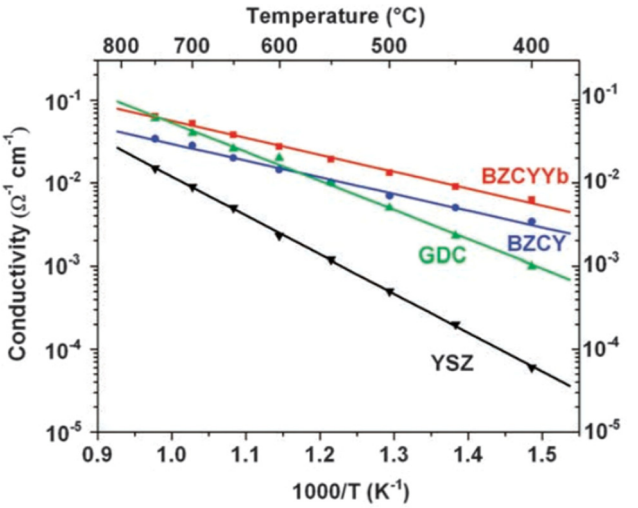

Fig. 3 Ionic conductivities of BZCYYb, BZCY, GDC, and YSZ as measured at 400° to 750 °C in wet oxygen (with ~3 vol % H_2O).[23]

hydration and thus proton conductivity, the B site needs to be partially doped by rare earth cations such as Y^{3+}, Yb^{3+}, Gd^{3+}, and Sm^{3+}. For example, Y- and Zr-doped $BaCeO_3$ ($BaCe_{1-x-y}Zr_xY_yO_{3-\delta}$, BCZY) has been one of the most studied systems for H^+ conductors with high conductivity and chemical stability under CO_2, H_2O, or H_2S-containing atmosphere.[29,30] Similarly, Y-, Zr- and Yb-triple-doped $BaCeZrO_3$ with compositions of $BaZr_{0.1}Ce_{0.7}Y_{0.2-x}Yb_xO_{3-\delta}$ (x = 0 to 0.2, BZCYYb) has also been reported with good ionic conductivity and chemical stability.[23] Fig. 3 shows the comparison of ionic conductivity in 3%H_2O moistened O_2 among BZCYYb, YSZ (Y_2O_3-stabilized ZrO_2), GDC (Gd_2O_3-doped CeO_2) and BZCY; it is evident that BZCYYb shows the highest conductivity below 750 °C.

The fuel cell performance with BZCYYb as an electrolyte was further demonstrated with a high faradaic efficiency (90–98%) and >97% overall electric-to-H_2 energy conversion efficiency (based on the lower heating value of H_2) at a current density of 1 A cm^{-2}.[22] With a co-fed CO_2 and H_2O, the same cell was shown with a round-trip efficiency (electricity-to-H_2-to-electricity) >75% and stable operation at a degradation rate of <30 mV per 1000 h.

A similar composition, $BaZr_{0.4}Ce_{0.4}Y_{0.1}Yb_{0.1}O_3$ (BZCYYb4411), has been tested as a H^+-conducting electrolyte in a solid oxide cell setting with a mixed conductor $PrBa_{0.5}Sr_{0.5}Co_{1.5}Fe_{0.5}O_{5+\delta}$ (PBSCF) as the air electrode, and a composite of Ni–BZCYYb4411 as the fuel electrode, see Fig. 4(a) and (b).[31] The low-temperature solid oxide fuel cell (SOFC) performance, see Fig. 4(c), is outstanding and the long-term steam electrolysis performance under 500 °C and constant 1.3 V, see Fig. 4(d), is also high and stable cells, further demonstrating the potential of $BaCeO_3$–$BaZrO_3$-based materials as a good H^+ conductor.

Despite the broad interest in perovskite H^+ conductors, practical applications of these conductors in large and thin film formats have been severely limited due to the poor mechanical strength, high reactivity with adjacent components, and difficult processing conditions. Therefore, how to implement the $BaCeO_3$–$BaZrO_3$-based H^+-conductors into solid oxide cell (SOC) stacks remain an engineering challenge.

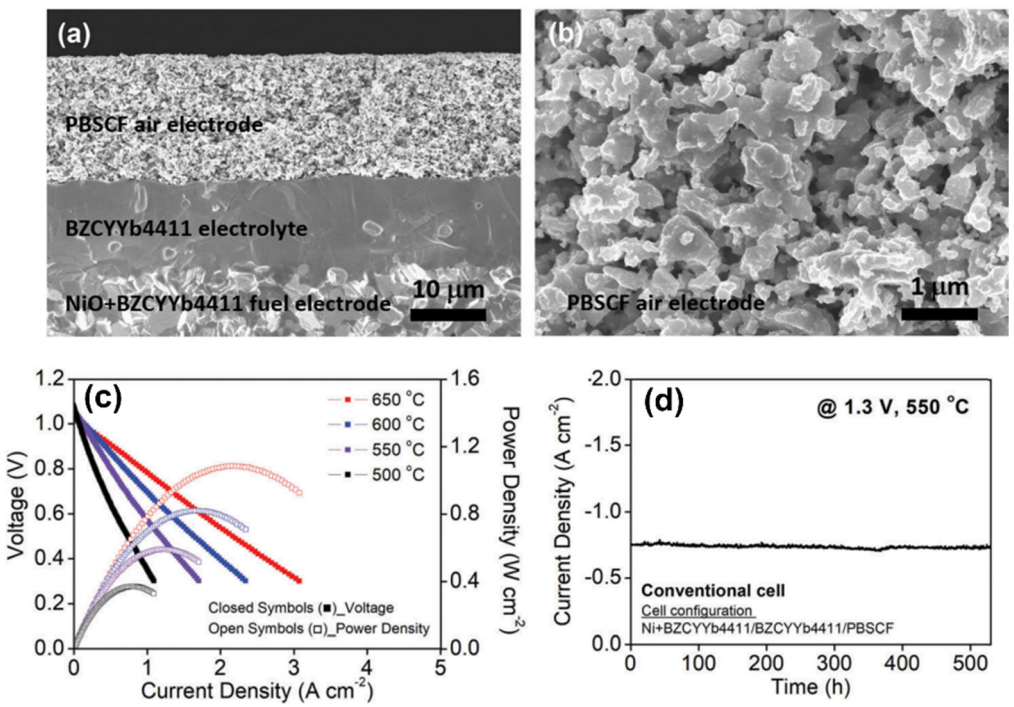

Fig. 4 (a) Cross-sectional view of 15 μm thick, dense electrolyte BZCYYb4411 and a 15 μm thick, porous PBSC air electrode supported on a porous fuel electrode. (b) Microstructure of the PBSCF air electrode. (c) *V–I* and *P–I* curves under fuel cell modes. (d) Long-term steam electrolysis performance at 550 °C and a fixed 1.3 V.[31]

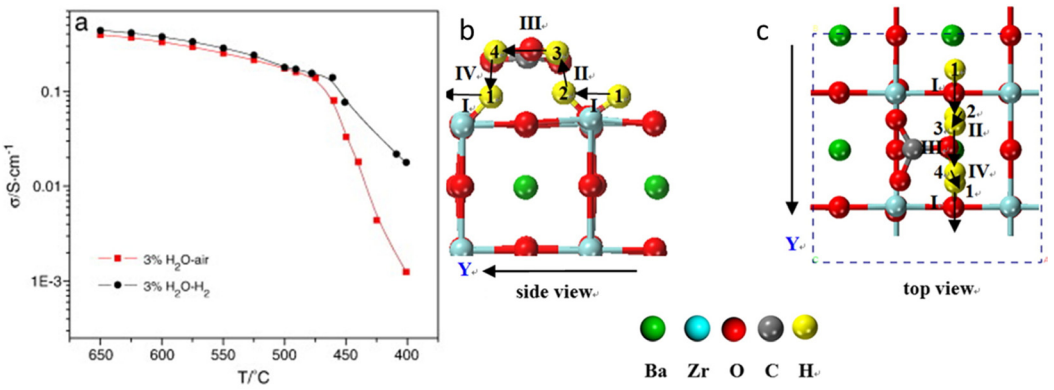

Fig. 5 Plots of effective ionic conductivity of BZY-$(Li_{0.62}K_{0.38})_2CO_3$ (MC) (a) *vs.* temperature in 3%H_2O–air and 3%H_2O–H_2.[32] Migration pathways for H^+-migration along the *Y* direction in MPCC, (b) side view and (c) top view. The migration pathways are marked with arrows.[33]

2.2 Perovskite proton conductors mixed with molten carbonate

To overcome the chemical stability issues and manufacturing difficulties associated with the BZY H^+-conductor, a mixed proton and carbonate ion conductor (MPCC) comprising of a pre-sintered proton conductor $BaZr_{0.8}Y_{0.2}O_{3-d}$ (BZY) skeleton infiltrated with molten carbonate (MC) phase was reported.[32] The H^+-conductivity of MPCC reached 0.33 S cm^{-1} at 600 °C in 3% H_2O–air and and 0.38 S cm^{-1} in 3%H_2O–H_2, which is roughly two orders of magnitude higher than pure BZY, see Fig. 5(a). With the aid of MC, not only is the H^+-conductivity of BZY improved, but also a fully dense microstructure is achieved by the MC phase.

To explain the conductivity enhancement at high temperature (*e.g.* T = 600 °C), a new mechanism based on defect reactions involved in the BZY and MC phases was proposed:

$$H_2O(g) + V_O^{\bullet\bullet} + (CO_3)_{CO_3}^{x} \leftrightarrow (OH)_O^{\bullet} + (HCO_3)_{CO_3}^{x} \qquad (3)$$

At the BZY/MC interface, simultaneous H^+ conduction takes place in the bulk BZY and along the interface of BZY/MC, where extensive H^+ exchange and transfer can occur. To support the above hypothesis, a density functional theory (DFT) was conducted on the system to map out the pathways and energetics of H^+ migration in BYZ/MC.[33] The calculations explicitly show that the H^+ migration prefers a curved pathway along the ZrO_2-terminated (110) surface in $BaZrO_3$, see Fig. 5(b) and (c). However, the MC phase provides an alternate, more conductive pathway for H^+ to migrate along the surface of $BaZrO_3$, thus facilitating the H^+ exchange between $BaZrO_3$ and MC phase across the interface. The study modeled H^+ migration in CO_3^{2-}, Li_2CO_3 crystals, and $(Li_2CO_3)_8$ clusters and show that the H^+ transfer in $(Li_2CO_3)_8$ clusters, a surrogate of MC, rather than in solid carbonates, is fast, confirming the feasible and fast H^+ transport in the MC phase.[34] Overall, the experimental and theoretical results suggest the potential application of dual-phase BYZ/MC MPCC as an electrolyte for intermediate-temperature solid oxide cells.

2.3 Ruddlesden–Popper oxides

The Ruddlesden–Popper (RP) oxides refer to the family with a general formula of $A_{n+1}B_nO_{3n+1}$, where $n \geq 1$; A is a rare-earth or an alkaline-earth element, and B is a transition metal.[35] The formula can also be otherwise viewed as $(AO)(ABO_3)_n$, where n is the number of connected layers of corner-sharing BO_6 octahedra. The structure is built of consecutive perovskite $(ABO_3)_n$ blocks alternating with rock-salt AO layers along the *c* crystallographic axis, see Fig. 6.

$Ln_2NiO_{4+\delta}$ (Ln = La, Nd, and Pr) is an n = 1 RP compound. They have recently attracted attention due to their low thermal expansion coefficients (TECs), high oxygen bulk diffusion and surface exchange coefficients, which makes them a good candidate for SOCs. While being oxide-ion conductive, $Ln_2NiO_{4+\delta}$ is also conductive to protons and electrons, thus expanding the active sites for electrochemical reactions.[37] Fig. 7 shows the possible crystallographic sites for H_2O insertion in $Ln_2MO_{4+\delta}$ (Ln = rare earth element) to produce protons *via* the following

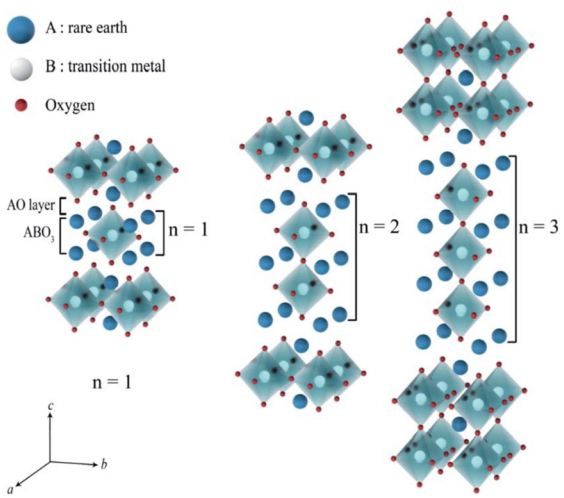

Fig. 6 Idealized representation of the crystal structures of Ruddlesden–Popper (RP) phases.[36]

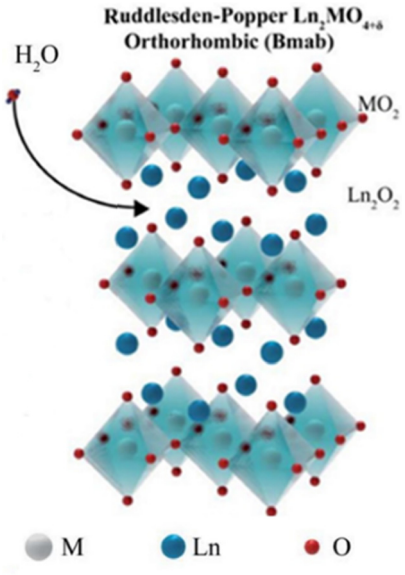

Fig. 7 The crystal structure of $Ln_2MO_{4+\delta}$ with the arrow indicating the possible water insertion sites.[36]

defect reaction:[36]

$$H_2O + O_O^{\times} \leftrightarrow OH_O^{\bullet} + OH_i' \quad (4)$$

Here, OH_i' represents H attached to the interstitial O and $OH_O^{\bullet}$ represents H attached to the lattice O. This mechanism is different from perovskite proton conductors mentioned above, where H_2O reacts with $V_O^{\bullet\bullet}$ to produce $OH_O^{\bullet}$. Here in the structure of $Ln_2NiO_{4+\delta}$, the interstitial O (O_i'') is a prevalent point defect. Therefore, it is envisioned that H^+ hops between $OH_O^{\bullet}$ and OH_i' to enable H^+ conduction. While the above mechanism still needs experimental verification, many studies agree that the H^+ conducting mechanism is different between RP and traditional perovskite oxides.

The applications of RP materials in H^+-conducting solid oxide electrolysis cells (SOECs) have been tried in laboratory studies. The results are sometimes contradicting. For example, an H^+-SOEC based on $BaZr_{0.2}Ce_{0.6}Y_{0.2}O_{3-\delta}$ (BZCY) electrolyte and $Pr_2NiO_{4+\delta}$ (PNO) anode was shown with good chemical compatibility and catalytic activity towards water splitting.[37] In another study on $Ln_2NiO_{4+\delta}$ (Ln = La, Pr, Nd) in steam and CO_2 environments, however, notable secondary hydroxides and carbonates were detected on the surface after being exposed to high steam pressure (40 bar) at 550 °C.[38]

Despite numerous early works, the H^+ transport mechanisms and properties in RPs are not well understood and attained as perovskite counterparts.[39] More comprehensive and in-depth studies are, therefore, needed for understanding H^+ conducting mechanisms and measuring H^+ conductivity in RP oxides in the future.

2.4 Pyrochlores

Pyrochlore oxides with the composition of $A_2B_2O_7$ have also been found to be proton conductive.[40–42] The acceptor doped $A_2B_2O_7$ have been shown with improved proton conductivity over the undoped $A_2B_2O_7$.[43] The doped $La_{1.95}Ca_{0.05}Zr_2O_7$ exhibits a total conductivity of 6.8×10^{-2} at 600 °C, see Fig. 8(a), in which partial H^+ conduction is dominating.[43] The oxygen vacancies created by the acceptor doping are the vehicles for proton conduction as illustrated by reaction (1). MD simulations support the necessity of acceptor doping in $A_2B_2O_7$ on either A- or B-site for long-range H^+ conduction.[44] Fig. 8(b) shows the structure of $La_2Zr_2O_7$, in which Zr ions (invisible in Fig. 8(b), embedded inside the octahedra) are located at the centers of the distorted octahedra and O ions (small, white balls) at their corners. The La ions (large, dark-shaded balls) together with O′ (medium-size, white balls) constitute an interpenetrating chain-like network. The suggested proton pathway is illustrated in Fig. 8(c) by following (ii) → (ii) → (v) → (v) → (ii) → (ii) → .... Notably, only sites (ii) and (v) must

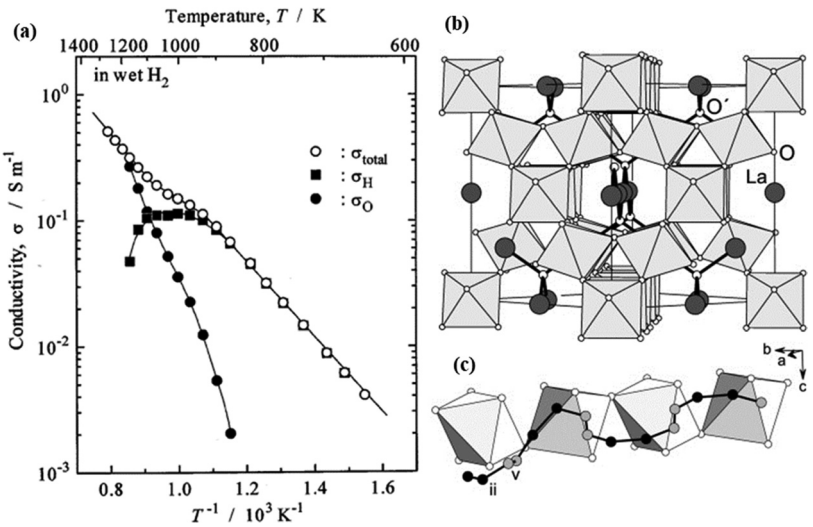

Fig. 8 (a) Arrhenius plot of conductivity of $(La_{1.95}Ca_{0.05})Zr_2O_7$ in wet H_2, (■) σ_H, (●) σ_O and (○) σ_{total} represent partial proton, oxide-ion conductivity, and total conductivity, respectively;[43] (b) $La_2Zr_2O_7$ structure; (c) suggested proton conduction pathway.[44]

be visited to form a continuous trajectory. The (ii) to (ii) separation is 1.54 Å, whereas (v) to (v) and (ii) to (v) are 0.76 Å and 1.22 Å, respectively. It is also found that negatively charged dopants are associated with H^+, and consequently, the proton diffusivity is hindered in their vicinity. However, the binding energy of the associate is quite small in the case of Sr and Ca, making them a reasonable conductor.[44]

Several applications using pyrochlores as electrolytes in fuel cells, hydrogen sensors, hydrogen separation membranes, and electrochemical ammonia synthesis have been demonstrated. However, the major issue for pyrochlores is the low ionic conductivity, high sintering temperature (>1600 °C), making their practical use in SOCs less attractive.

2.5 Rare-earth *ortho*-niobates and *ortho*-tantalates

The rare-earth *ortho*-niobates and *ortho*-tantalates refer to AMO_4 (A = rare earth; M = Nb, Ta). With 1% Ca acceptor doping, $RE_{1-x}A_xMO_4$ exhibits prominent proton conductivity in wet atmospheres below 800 °C. The highest proton conductivity was observed in 1% Ca-doped $LaNbO_4$, which was on the order of 10^{-3} S cm^{-1} at 800 °C, see Fig. 9(a).[45] However, this class of material experiences monoclinic fergusonite-type structures to tetragonal scheelite-type structures as temperature increases. The proton conductivity suffers a sudden drop as the structure is transformed from a tetragonal to a monoclinic structure, see Fig. 9(a).

In addition, the proton mobility in rare-earth *ortho*-niobates and *ortho*-tantalates is found to decrease with decreasing ion size, which is understandable because it leads to decreased lattice parameter, the polarizability of the lattice and proton-hosting oxygen sublattice. Typically, the smaller, stiffer lattices give rise to a less dynamic oxygen lattice, leading to its lowered momentum to match proton transfer. The proton mobility is also thought to be favored by the symmetry of the lattice.[46]

Using DFT method, the in-plane H^+-migration pathways in tetragonal $LaNbO_4$ are identified, see Fig. 9(b), in which H^+ diffuses by an inter-tetrahedral mechanism within a cation sublattice.[47] Briefly, pathways 1 and 2 show the proton rapidly shift position between two adjacent a sites and b sites, respectively, with a comparable potential barrier (0.04 eV and 0.06 eV, respectively) for so-called ''oscillatory proton transfer''. Pathway 3 is the additional migration path connecting a and b sites for long-distance proton migration within the plane with the third lowest potential barrier of 0.41 eV. It is also found that the proton rotates around the oxide ion before and after it jumps between the two tetrahedrons, *i.e.* rotation and hopping, which has also been found computationally in other proton conducting oxides, such as $BaCeO_3$ and $BaZrO_3$. For the out-of-plane proton migration, pathway 4 describes proton migration between two layers with a higher potential barrier of 0.74 eV. So far, only a few literature are available on the proton conductivity in rare-earth *ortho*-niobates and *ortho*-tantalates, leaving great space for future exploration of this class of materials.

3. Solid polyanionic salts as proton conductors

3.1 Sulfates

Solid sulphates such as Li_2SO_4, $Li_2Mg(SO_4)_2$, $LiAgSO_4$, and Rb_2SO_4 were first found to be proton conducting in the early 1970s.[48] Among these, Li_2SO_4 exhibits proton conductivity in its α-phase stable between 577 °C (first-order transition temperature) and 860 °C (melting temperature). The proton conducting α-phase has a face centered cubic structure with a space group of *Fm*3*m*, see Fig. 10(a). It was later discovered that the first-order transition temperature of the proton-conducting phase could be reduced to ~450 °C by adding a small amount of Al_2O_3 into Li_2SO_4.[50,51]

The mechanism of proton conduction follows the paddle wheel model,[49] in which steps of proton-attachment to SO_4^{2-}, *i.e.* $(H\text{-}SO_4)^-$, rotation of SO_4^{2-}, and pushing-out of H^+/Li^+ are considered, see Fig. 10(a). The proof of proton conductivity was provided by hydrogen concentration cells. The cell with

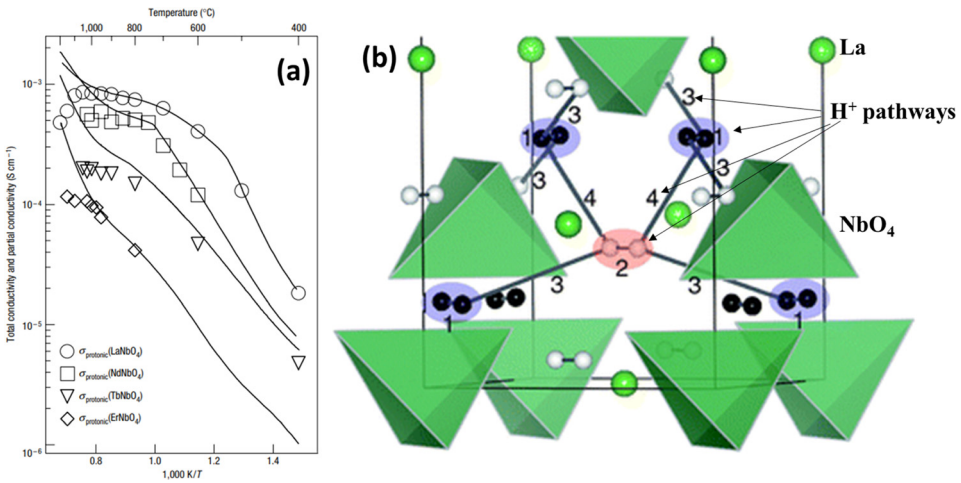

Fig. 9 (a) Protonic conductivities of 1% Ca-doped $RENbO_4$;[45] (b) proton migration paths with low potential barriers in the tetragonal phase of $LaNbO_4$. Proton migration pathways are labelled as 1–4 in the figure.[47]

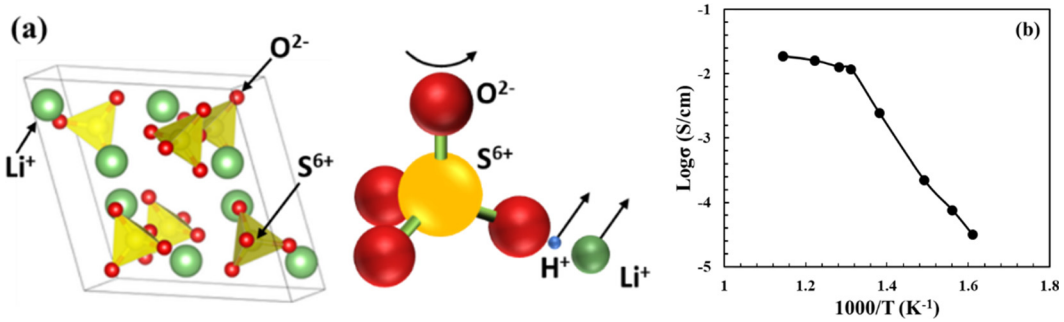

Fig. 10 (a) Crystal structure of the face-centered cubic α-Li_2SO_4, where SO_4 tetrahedron and its rotation pushing out of Li^+ and H^+ are illustrated.[49] (b) Arrhenius plot of proton conductivity of Li_2SO_4-45 mol%Al_2O_3 (reproduced from ref. 50).

Li_2SO_4–Al_2O_3 as the electrolyte showed zero EMF (electromotive force) in O_2 atmospheres, but proportional to the logarithm of partial pressure of H_2.[50] A high proton conductivity in the order of 10^{-2} to 10^{-1} S cm^{-1} has been observed in α-Li_2SO_4, see Fig. 10(b).[50]

3.2 Nitrates

Like solid sulphates, solid nitrates (MNO_3, M = Li, Na, K, Rb, Cs, *etc.*) were also found to exhibit high proton conductivity. It was also found that proton conductivity increases with crystallinity of nitrates and cationic radius as a result of the soft M–O bonds and open crystal structures.[52] To stabilize and increase the conductivity of MNO_3, Al_2O_3 is often added. The conductivities of $RbNO_3$–Al_2O_3 and $CsNO_3$–Al_2O_3 measured by hydrogen concentration cells are comparable to Li_2SO_4–Al_2O_3, in the order of 10^{-2} to 10^{-1} S cm^{-1} above 400 °C, see Fig. 11(a).[53] For face-centered cubic $RbNO_3$, for example, protons migrate through the interfacial coordinative mechanism between $RbNO_3$ and Al_2O_3, see Fig. 11(b).

The major drawbacks of solid sulphates and nitrates, however, are their weak mechanical strength and low chemical and electrochemical stability, as they could decompose at higher temperatures if not properly stabilized. For instance, nitrates may decompose at a temperature >350 °C,[54] while sulphates may undergo reduction to form H_2S and H_2O in H_2-containing atmospheres.[55] These drawbacks have limited the practical applications of solid sulphates and nitrates.

3.3 Pyrophosphates

Compared to sulphates and nitrates, phosphates or complex heteropolyacids, such as pyrophosphates, have a better chemical stability. An early study by Zhu *et al.* suggests that K_3PO_4–Al_2O_3 with a cubic α-phase similar to sulphates and nitrates has a proton conductivity of 10^{-3} to 10^{-2} S cm^{-1} at a temperature above 550 °C.[50] A series of studies have also shown that Sr or Ca doped rare earth phosphates ($LnPO_4$, Ln = La, Ce, Pr, Nd, and Sm) exhibit high proton conductivity under wet reducing conditions.[56–60]

The protons' conduction mechanisms in doped phosphates are generally understood as follows:[58]

$$Sr_2P_2O_7 \rightarrow 2Sr'_{La} + (P_2O_7)^{\bullet\bullet}_{PO_4} \quad (5)$$

$$(P_2O_7)^{\bullet\bullet}_{PO_4} + H_2O(g) \leftrightarrow 2(HPO_4)^{\bullet}_{PO_4} \quad (6)$$

where Sr'_{La} represents Sr dopant on the La-lattice; $(P_2O_7)^{\bullet\bullet}_{PO_4}$ represents $(P_2O_7)^{4-}$ residing on the $(PO_4)^{3-}$ lattice; $(HPO_4)^{\bullet}_{PO_4}$ represents proton species residing on the $(PO_4)^{3-}$ lattice. Assisted by ^1H and ^{31}P magic angle spinning-nuclear magnetic resonance (MAS-NMR) and Fourier transform (FT)-Raman spectroscopy measurements, the formation of

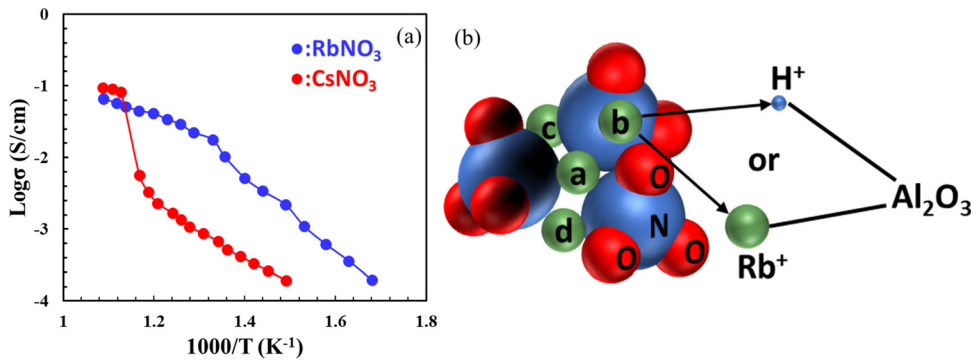

Fig. 11 (a) Arrhenius plot of proton conductivity for $CsNO_3$- and $RbNO_3$–Al_2O_3 composites (reproduced from ref. 52); (b) a schematic showing bonding between the M^+ and NO_3^- may be broken, which provides a coordination site for the proton. Thus, both Rb^+ and H^+ may stay at the interface between two phases in the $RbNO_3$–Al_2O_3 system; here a, b, c, and d represent four non-equivalent M-sites around NO_3^- (reproduced from ref. 53).

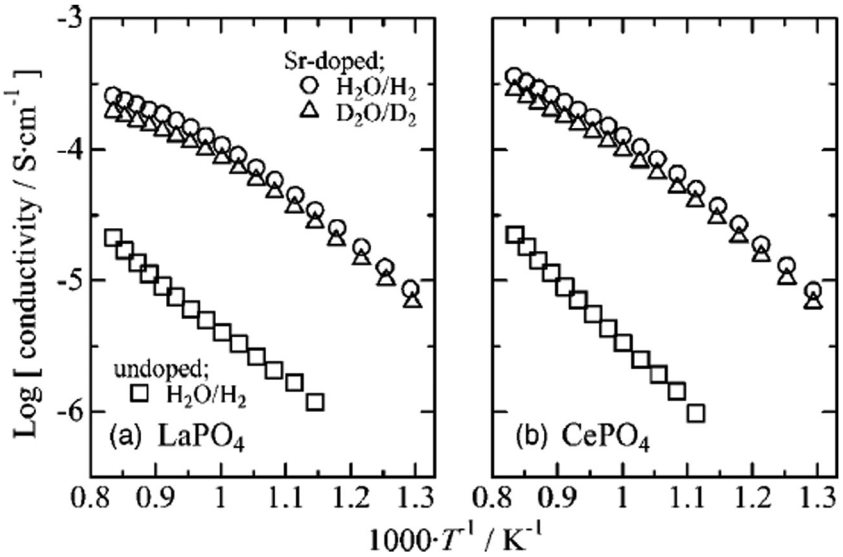

Fig. 12 Conductivities of undoped and 1 mol % Sr-doped (a) $LaPO_4$ and (b) $CePO_4$ under wet reducing conditions; pH_2O or pD_2O = 4.2 kPa, and pH_2 or pD_2 = 3 kPa.[56]

pyrophosphate ions $(P_2O_7)^{\bullet\bullet}$ at adjacent orthophosphate ions $(PO_4)^{3-}$ induced by the doping of Sr^{2+} into La^{3+} has been confirmed, which becomes the active site for water incorporation and the formation of $(HPO_4)^{2-}$ at $(PO_4)^{3-}$ sites, resulting in proton conduction.

The conductivities of 1 mol% Sr-doped $LaPO_4$ and $CePO_4$ reached $10^{-5.2}$–$10^{-3.5}$ S cm^{-1} and $10^{-5.2}$–$10^{-3.4}$ S cm^{-1}, at 500–925 °C, respectively, under H_2O/H_2 and D_2O/D_2 atmospheres (pH_2O = 4.2 kPa and pH_2 = 3 kPa); the results are shown in Fig. 12.[56] The lowered conductivity in D_2O/D_2 indirectly confirmed the nature of proton conduction in these materials.

In addition to phosphates, solid acid pyrophosphates TP_2O_7 (T = Sn, Ti, Si, Ge, Ce, and Zr) have also been found to exhibit proton conductivity in the order of 10^{-3} to 10^{-2} S cm^{-1} within 100 to 400 °C under anhydrous conditions.[61–64] The pyrophosphates typically have a face centered rock salt cubic structure with TO_6 and P_2O_7 units sharing corners, see Fig. 13(a). Moreover, Nagao *et al.* reported that partial substitution of In^{3+} for Sn^{4+} in SnP_2O_7 can improve the proton conductivity from 5.56 × 10^{-2} to 1.95 × 10^{-1} S cm^{-1} at 250 °C, see Fig. 13(b).[65] By studying the H/D isotope effect, the proton conduction in TP_2O_7 was proposed to follow the hopping mechanism, *i.e.*, migration *via* dissociation of O–H bonds. Moreover, it was also found that the presence of P_2O_7 ions has a deficiency in the lattice of TP_2O_7, leading to a lower proton conductivity than undoped pyrophosphates, due to the decrease in proton mobility.

The improved stability of phosphates and pyrophosphates, compared to solid sulphates and nitrates, makes them more

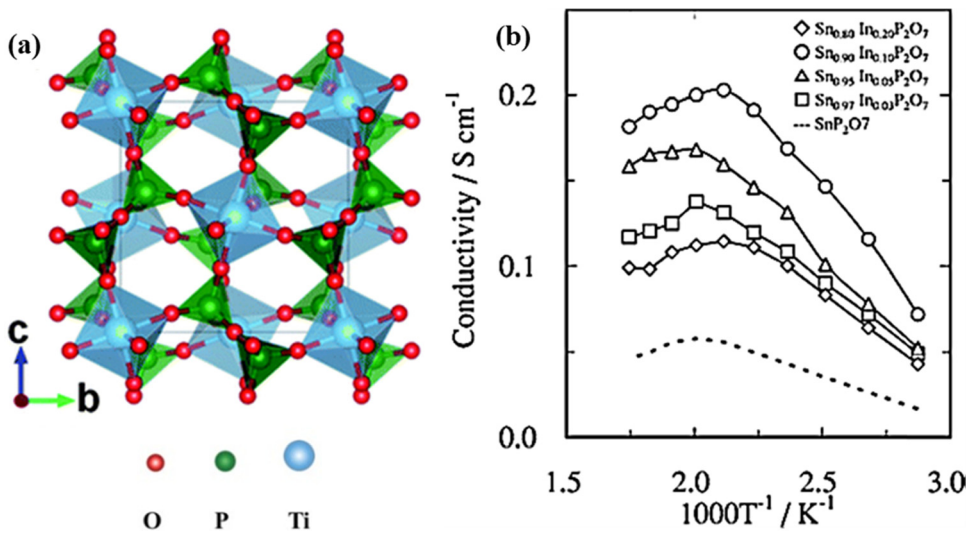

Fig. 13 (a) Crystal structure of TiP_2O_7,[66] TiO_6 octahedra and PO_4 tetrahedra are shown in blue and green in color, respectively, and (b) Arrhenius plot of the conductivity of $Sn_{1-x}In_xP_2O_7$ in dry air (pH_2O = ~0.0075 atm).[65]

practical. Recently, the use of pyrophosphates composite electrolytes has drawn attention due to their stability in a wider voltage and temperature range. For example, Hibino *et al.* reported that the $Sn_{0.95}Al_{0.05}H_{0.05}P_2O_7$ (SAPO)-polytetrafluoroethylene (PTFE) composite shows a high proton conductivity of 0.02 S cm^{-1} at 200 °C with a highly condensed H_3PO_4 electrode ionomer in a supercapacitor configuration. Such an electrolyte also exhibits a wide voltage range of ±2 V. The resultant performance of such a supercapacitor reaches an energy density of 32 W h kg^{-1} at 3 A g^{-1} and stable 7000 cycles from room temperature to 150 °C.[67] Given their relative low cost and ease of preparation, they remain an attractive class of proton conductors for future consideration.

3.4 Solid acids

A group of solid acids, $MHAO_4$ and $M_3H(AO_4)_2$ with monovalent alkali metal cations M = Rb, Cs, NH_4 and tetrahedral oxyanions AO_4 (A = S, P, Se) exhibits super proton conductivity above a phase transition temperature between 50 and 250 °C even in a dry atmosphere. This class of material was first reported by Baronov *et al.*,[68] in which high proton conductivity (10^{-3}–10^{-2} S cm^{-1} at 140–230 °C) was observed in $CsHSO_4$ and $Rb_3H(SeO_4)_2$, see Fig. 14(a). The high proton conductivity was attributed to the unique proton disorder in H-bond networks. CsH_2PO_4 was found later to have a higher transition temperature (230 °C) and decomposition temperature (375 °C in high humidity) than $CsHSO_4$ (140 °C and 200–230 °C, respectively) and exhibit a higher proton conductivity of 2.2×10^{-2} S cm^{-1} at 200 °C and 4.0×10^{-2} S cm^{-1} at 240 °C, respectively.[69] The proton conduction mechanism in these acids follows successive intra-bond jumps, reorientations of the O–H group and breaking of an old H-bond and forming of a new one, see Fig. 14(b).[70]

The potential of phosphate-based solid acids for application in fuel cells has been shown by Haile *et al.*[55] With a thick $CsHSO_4$ membrane (thickness: ~1.5 mm) as the electrolyte, the work showed a promising OCV of 1.11 V, and output of 44 mA cm^{-2} at 150 °C. With a 25 μm thick CsH_2PO_4 as an electrolyte film, the fuel cell produced a peak power density of 415 mW cm^{-2} at 240 °C under humidified (pH_2O = 0.3 atm) H_2 and pure O_2.[69] However, a further application of solid acids in fuel cells is limited by the strict operating conditions (*e.g.* high humidity and narrow temperature range). Similar to pyrophosphates, a combination of solid acids with a metal–organic coordination framework shows promising conductivity and stability, especially under low humidity. For example, Ponomareva *et al.* reported that a composite of $CsH_5(PO_4)_2$ and a metal–organic coordination framework, Cr-MIL-101 matrix, exhibits a conductivity of ~10^{-2} S cm^{-1} at 130 °C at RH = 10–15%.[71] The high proton conductivity under low RH suggests that the hybrid solid acids composite could find potential applications in fuel cells and H_2 pumps.

4. Hydrates as proton conductors

The materials that become proton conductive when they are in a fully hydrated state are classified as proton-conducting hydrates. Since this class of materials relies upon the degree of adsorbed water to conduct protons, their operating temperature is typically low.

4.1 Mesoporous nanocomposites

Some mesoporous inorganic materials with nanosized pores in 2 to 50 nm become proton conductive due to physically adsorbing water molecules. Yamamda *et al.* reported an inorganic TiO_2–P_2O_5 mesoporous nanocomposite with a proton conductivity of 10^{-2} S cm^{-1} at 160 °C, under fully saturated humidification conditions, see Fig. 15.[72] The high proton conductivity is attributed to the strong P-POH chemisorption enabled by P_2O_5 under high humidity conditions.[73]

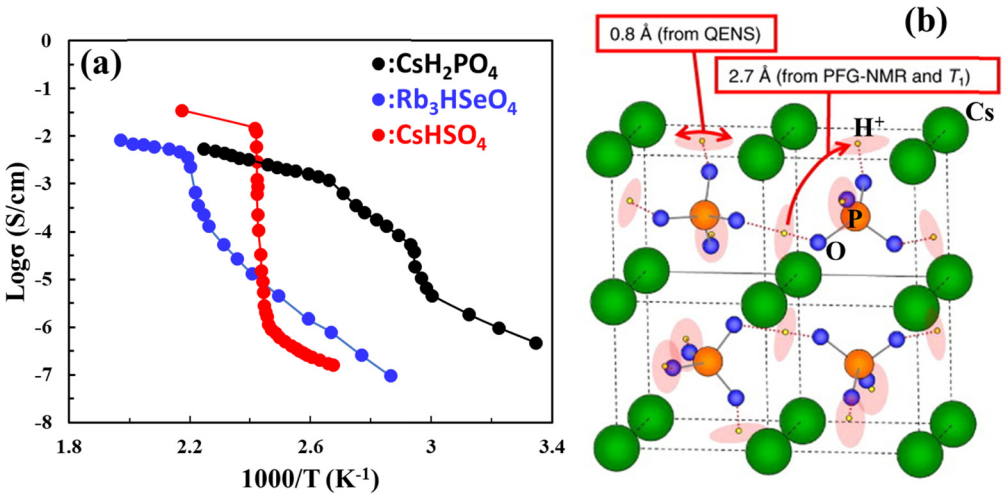

Fig. 14 (a) Arrhenius plot of proton conductivity of CsH_2PO_4, Rb_3HSeO_4, and $CsHSO_4$ (reproduced from ref. 55) and (b) illustration of two proton diffusion movements in CsH_2PO_4, confirmed *via* ^1H pulsed field gradient NMR, ^1H NMR spin-lattice relaxation time (T_1), and quasi-elastic neutron scattering measurements.[70]

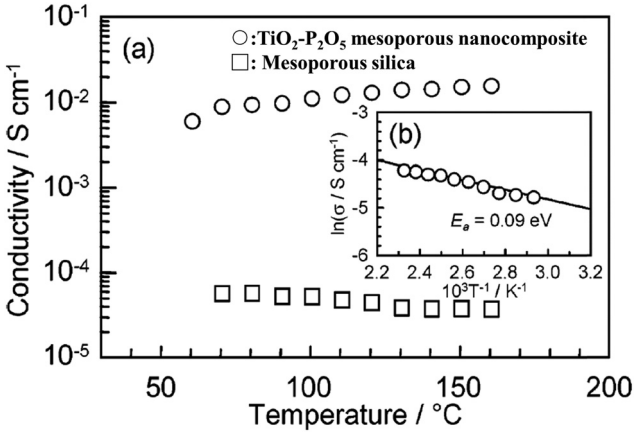

Fig. 15 (a) Proton conductivity of (○) TiO_2–P_2O_5 mesoporous nanocomposites and (□) mesoporous silica measured from the RT to 160 °C under 100% relative humidity (RH) conditions. (b) Arrhenius plots of the conductivity of the TiO_2–P_2O_5 mesoporous nanocomposites. A solid line is the least-squares fitting. The activation energy (E_a) of the proton transport was estimated from the slope. Reprinted with permission from *J. Am. Chem. Soc.*, 2005, **127**(38), 13092–13093. Copyright (2007) American Chemical Society.[72]

Similarly, Marschall *et al.* reported that highly ordered mesoporous silicas with sulfonic acid groups (SO_3H) when combined with Nafion to form a functional group (Si-MCM-41, Mobil Composition of Matter No. 41) exhibited very high proton conductivity up to 0.2 S cm^{-1} under fully saturated humidification conditions.[74] The high proton conductivity in the presence of water is derived from the Grotthus mechanism, see Fig. 16.[75] In this mechanism, the proton transport is realized by protons hopping from one water molecule to another. To a smaller extent, the diffusion of H_3O^+ also enhances proton transport. At higher temperatures, hopping and diffusion become faster since the rotation and vibration of anchoring propyl chains increase, allowing the SO_3H groups at the end of the chains to encounter each other more freely, thus facilitating the direct proton transport. A recent study by Vinothkannan *et al.* shows substantially high proton conductivity (45.1 mS cm^{-1}) under RH = 50% and 120 °C for the optimized Nafion/SO_3H-1 wt% unzipped graphite nanofiber (UGNF) membrane.[76]

In contrast to Nafion fouls, for which the proton conductivity decreases drastically above 100 °C due to the water loss, water seems to be kept inside the channels of mesoporous nanocomposites due to the geometry of the pores which fixes the sulfonic acid groups, thus maintaining proton conductivity even at higher than 100 °C. It was also found that the proton conductivity increased with the extent of substitution of metasilicate with MCM. The highest proton conductivity of 0.2 S cm^{-1} was achieved with a 40% SO_3H-MCM-41 (mw) sample due to the high pore filling with SO_3H groups and the absence of parasitic pores.

4.2 Heteropolyacid hydrates

Early studies have found that some heteropolyacids in a hydrated state, such as $H_4SiW_{12}O_{40}{\cdot}28H_2O$, $H_3PW_{12}O_{40}{\cdot}29H_2O$, and $H_3PMo_{12}O_{40}{\cdot}29H_2O$, exhibit high proton conductivity.[77–79] The proton conductivities are in the order of 10^{-2} and 10^{-1} S cm^{-1} at room temperature. Large and globular anions (*e.g.* $[Mo_{12}PO_{40}]^{3-}$) with Keggin structures are present in these hydrates, with crystal water showing violet thermal motion which can be easily dehydrated and rehydrated. These crystal waters contribute to the high proton conductivity, but only within a narrow window. Temperature and humidity are key factors in maintaining stable hydrates, where 80 °C and 70–80% RH are typically required conditions. In addition, pelletization or other processing methods can lead to the loss of crystallization in these hydrates. Thus, some porous oxides such as SiO_2 and Al_2O_3 have been often used as a matrix to reinforce the stability and robustness of heteropolyacid hydrates, which makes their application in solid electrolytes, sensors, and electrochromic displays possible.[80,81]

4.3 Layered hydrates

Another group of hydrates studied as a proton conductor has a layered structure. Examples include $HUO_2PO_4{\cdot}4H_2O$,[81] α-$Zr(HPO_4)_2{\cdot}nH_2O$,[82] γ-$Zr(PO_4)(H_2PO_4){\cdot}2H_2O$,[83] and γ-Zr sulfoaryl phosphonates.[84] They are acid groups that exhibit high

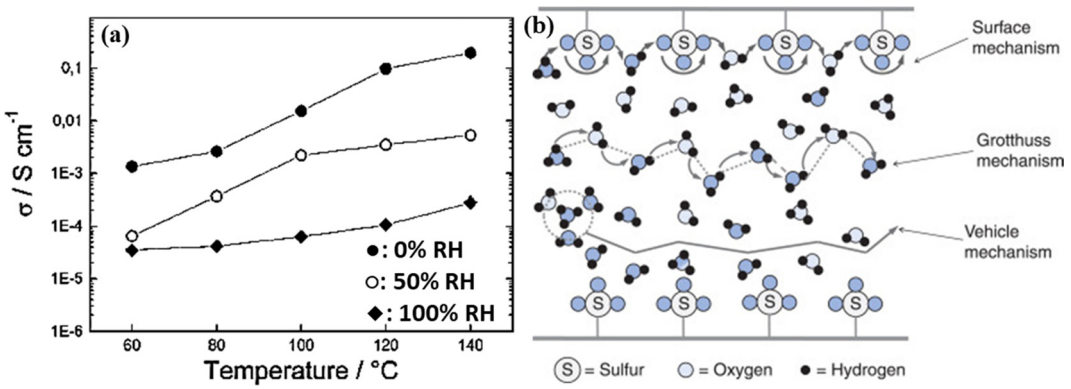

Fig. 16 (a) Proton conductivity of 40% SO_3H-MCM-41 (mw) at 0% (◆), 50% (○), and 100% (●) RH, Reprinted with permission from Chem. Mater. **19**, 26 (2007): 6401–6407. Copyright (2007) American Chemical Society.[74] and (b) simplified schematic representation of proton transport *via* the surface mechanism, Grotthuss mechanism, and vehicle mechanism.[75]

proton conductivity of 10^{-4} to 10^{-2} S cm^{-1} over a wider temperature range, but thermally more stable than heteropolyacids hydrates. In these compounds, a phase transition occurred above ~50 °C,[85] resulting in a significant increase in proton conductivity, due to the formation of an interlamellar H-bonded network with abundant H_3O^+ and high concentration of H^+.

The conduction mechanism is similar to that in mesoporous nanocomposites, with a hybrid Grotthuss-vehicle mechanism involving an intermolecular transfer (hopping) and an intramolecular transfer of protons. The former could be facilitated by the high concentration of H_3O^+ in the structure, and the latter is most likely facilitated by the high concentration of H-bond vacancies.

Some oxides, such as Sb_2O_5,[86] SnO_2,[87] V_2O_5, ZrO_2[88] and VO_2,[89] are also found to be proton conductive in their hydrated states. Proton conductivities of 10^{-4} to 10^{-2} S m^{-1} are found below 300 °C. Typically, maintaining saturated water vapor pressure is required to achieve sustainable proton conductivity. The proton conduction in such hydrates typically follows a pathway involving first, rotation around the O atom, and then migration between O atoms, see Fig. 17.

Despite the high proton conductivity of all these hydrates, their practical application is still limited due to the difficulty of retaining water and poor thermal stability during operation.

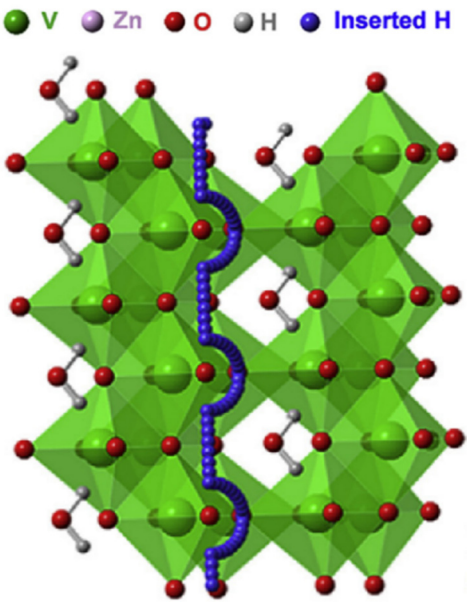

Fig. 17 Migration pathways for H^+ in H-VO_2.[89]

5. Hydrides as hydride-anion conductors

In chemistry, a hydride is formally an anion of hydrogen, H^-. Therefore, hydrides often refer to compounds and ions in which hydrogen is covalently attached to a less electronegative element. In such cases, the H center has a nucleophilic character, which contrasts with the protic character of acids.

5.1 Hydrides

Early studies revealed that some alkaline earth metal hydrides, such as CaH_2 and SrH_2, exhibit hydride anion (H^-) conductivity up to 10 S cm^{-1} above 780 °C,[90] and application of such materials as electrolytes for fuel cells was also reported.[91] More recently, a study on BaH_2/BaD_2 by Verbraeken *et al.* suggested that the high proton conductivity was attributed to H^- and achieved in a Ni_2In-type structure transformed from a cotunnite structure at ~470 °C, where a sharp increase in conductivity was observed.[92] The phase transition from cotunnite to high-symmetry Ni_2In type structures was also promoted by high pressure. A large concentration of hydride vacancies was also observed in the structure with a composition of roughly $BaH/D_{1.84}$, which contributes to the proton conductivity. In addition, small Ba-to-H or deuteride bond length, high isotropic temperature factors for D1 and D2 (7.6 and 11.6 Å), small mass and high mobility of D ions, see Fig. 18(a), all give rise to the superionic conductivity in BaD_2. The conductivity of BaH_2 is in the range of 0.04–0.2 S cm^{-1} between 470 and 630 °C, see Fig. 18(b).

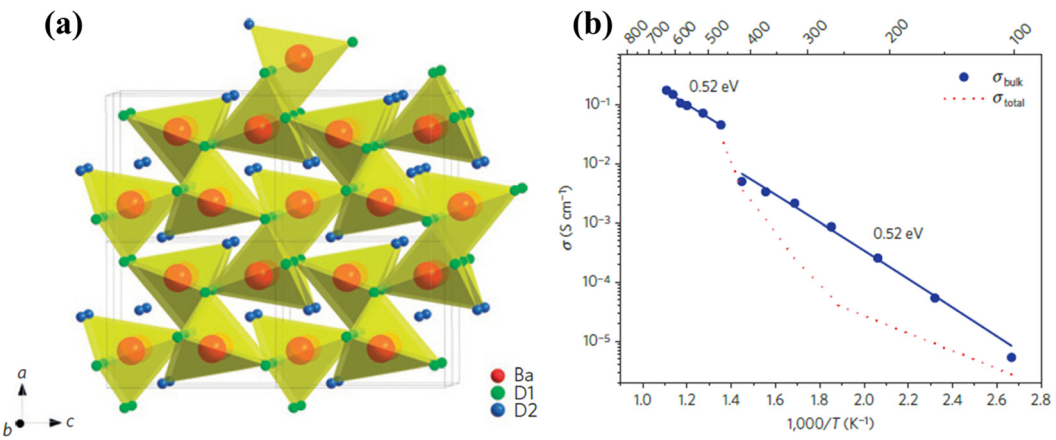

Fig. 18 (a) Crystal structure of BaD_2, and (b) Arrhenius plot of hydride-anion conductivity of BaH_2.[92]

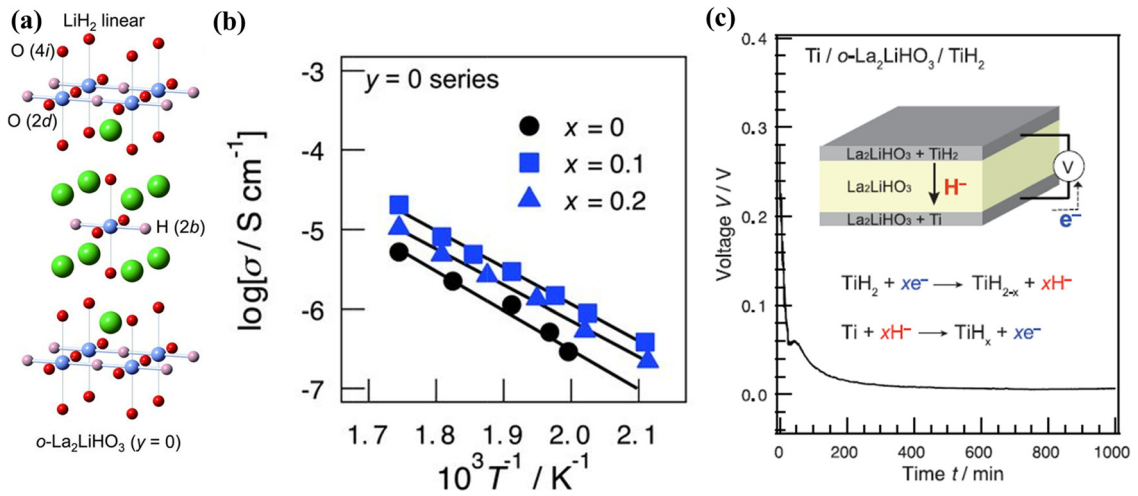

Fig. 19 (a) The crystal structure of o-$La_2LiH_3O_3$, (b) Arrhenius plot of the ionic conductivity of $La_{2-x}Sr_xLiH_{1-x}O_3$ (y = 0, 0 ≤ x ≤ 0.2), and (c) discharge curve of cell Ti/o-La_2LiHO_3/TiH_2. The inset shows the cell configuration and the proposed electrochemical reactions.[95]

Despite the high hydride anion conductivity, the narrow operation window largely restricts the practical application of BaH_2. More recently, Ubukata *et al.* reported a solid solution of $Ba_{2-\delta}H_{3-2\delta}X$ (X = Cl, Br, or I) with a layered anion-ordered structure, which exhibited excellent hydride conductivity at low temperatures (*e.g.* 1 mS cm^{-1} at 200 °C).[93] The layered anion ordering and Schottky defects in such materials likely suppress the structural transition commonly occurring during cooling, thus retaining a highly symmetric hexagonal lattice at lower temperatures for H^- conduction. Furthermore, $AELiH_3$ (AE: alkaline earth metals) perovskites are also found to exhibit high H^--conduction at low temperatures (*e.g.* 5.0×10^{-6} S cm^{-1} at room temperature for $Sr_{0.925}Na_{0.075}LiH_{2.925}$),[94] implying that the employment of aliovalent cations on the A site in perovskite-type hydrides leads to the formation of hydrogen vacancies, thus enabling fast H^--conduction even at very low temperatures. These new discoveries widen the potential of hydrides for applications over a wider temperature range.

5.2 Perovskite and fluorite-type oxyhydrides

Perovskite and fluorite-type oxyhydrides containing H^- in the lattice, such as $La_{2-x}Sr_xLiH_{1+x}O_{3-x}$,[95] Ba_2ScHO_3,[96] $LaSrCoO_3H_{0.7}$,[97] *etc.*, have been shown to conduct H^- in a similar manner to the above BaH_2 hydrides. Kobayashi *et al.* reported that rare-earth lithium oxyhydrides of $La_{2-x-y}Sr_{x+y}LiH_{1-x+y}O_{3-y}$ conduct H^- over oxygen sublattices. One of the promising compositions, La_2LiHO_3, has been successfully synthesized into a K_2NiF_4-type structure with an orthorhombic structure at 923 K and 2 GPa for 30 min. In this structure, both H^- and O^{2-} are ordered on the axial anion sites, see Fig. 19(a). The

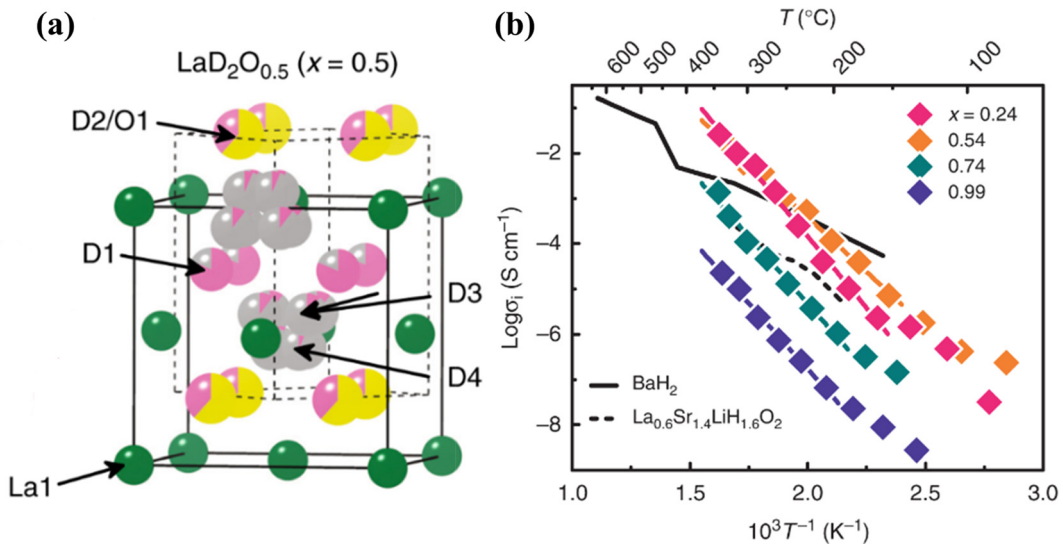

Fig. 20 (a) Crystal structure of $LaD_2O_{0.5}$ determined by NPD. Solid and dashed lines represent the unit cells of the FCC and tetragonal structures, respectively. Green, pink, yellow, and grey colors denote the fractions of La^{3+}, D^-, O^{2-}, and vacancies at each crystallographic site, respectively, and (b) Arrhenius plots of $LaH_{3-2x}O_x$ and H^- conductivity measured by AC impedance spectroscopy.[100]

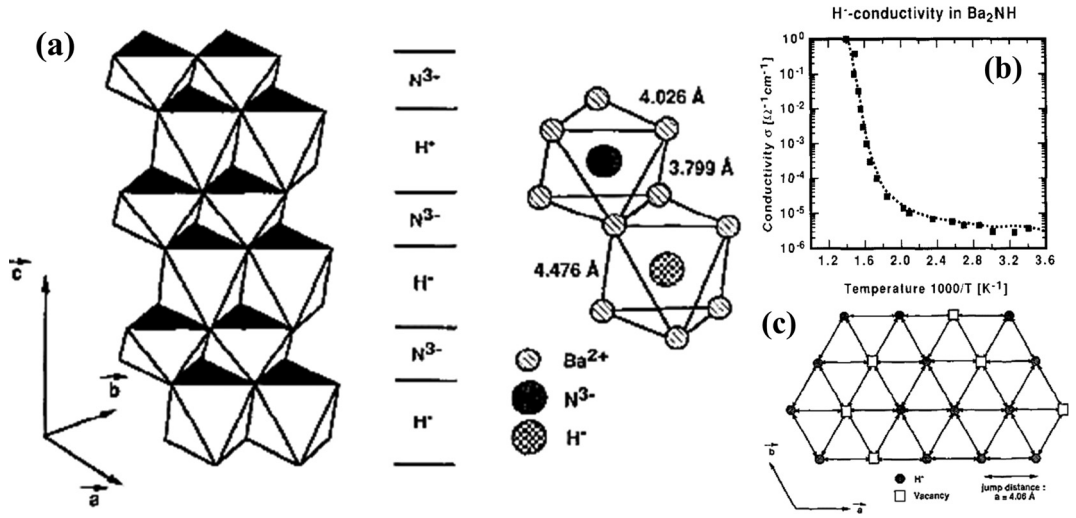

Fig. 21 (a) Layered type structure of Ba_2NH with distorted Ba-octahedra centered alternately by H^- and N^{3-}, with corresponding distance, (b) Arrhenius plot of H^- conductivity in Ba_2NH, and (c) diffusion of hydride anions in Ba_2NH *via* uncorrelated jumps between regular hydrogen sites.[101]

conductivity of $La_{2-x}Sr_xLiH_{1-x}O_3$ series ($0 \leq x \leq 0.2$, $y = 0$) is shown in Fig. 19(b), suggesting that Sr-induced vacancies increase H^- conductivity. With La_2LiHO_3 as the electrolyte, a cell consisting of Ti/*o*-La_2LiHO_3/TiH_2 has been constructed and tested; the results are shown in Fig. 19(c).[95] The cell exhibited an initial open circuit voltage of 0.28 V at 300 °C, consistent with the theoretical value of a Ti/TiH_2 redox couple. Under a constant discharge current of 0.5 mA, a steep drop-off in the cell voltage from 0.28 to 0.06 V was observed for the first reaction step, corresponding to the increase in the H^- content at the anode, followed by the cell voltage decreasing gradually to 0.0 V as H^- was continued added into Ti, implying the reaction between H and Ti was completed.

The synchrotron XRD indicates that the La_2LiHO_3 electrolyte is stable when in contact with the Ti and TiH_2 electrodes during the reaction, while phase changes were detected for both the cathode and anode. In the cathode, the initial δ-TiH_2 phase was found to transform into α-Ti upon releasing hydrogen; the corresponding lattice shrinkage was confirmed by the shift to a higher 2θ in the XRD pattern.

A more recent work shows that Ba–Li oxyhydride, $Ba_{1.75}LiH_{2.7}O_{0.9}$, synthesized under ambient pressure with a K_2NiF_4-type structure exhibited a high H^- conductivity ($\sim 10^{-2}$ S cm^{-1} at 300 °C) after an order–disorder transition.[98] Overall, H^- conductivity in such oxide-based framework structures is found to be almost independent of temperature but closely related to the anion ordering and vacancies.

Other than the H^--conducting oxyhydrides, mixed-electronic and ionic conductivity was also found in some oxyhydrides such as $BaTiO_{3-x}H_x$.[99] The high electronic conduction (*e.g.* 10^{-4} S cm^{-1} at 25 °C in $BaTiO_{2.4}H_{0.6}$) might find these materials as electrodes in an electrochemical cell.

Fluorite-type oxyhydrides are another group of hydrides with high H^- conductivity comparable to perovskite oxyhydrides. $LaH_{3-2x}O_x$ ($x = 0.54$) demonstrates the highest H^--conductivity of 2.6×10^{-2} S cm^{-1} at $T = 342$ °C, see Fig. 20.[100] The crystal structure of $LaD_2O_{0.5}$, an isotopic analogue of $LaH_2O_{0.5}$, is tetragonal, as determined by neutron powder diffraction (NPD). The light mass and large polarizability of H^- and the framework comprising of densely packed H^- in $LaH_{3-2x}O_x$ are crucial factors that enable significant temperature dependence of the H^- conductivity.

The successful demonstration of an all-solid-state electrochemical cell using oxyhydrides as an electrolyte presents the

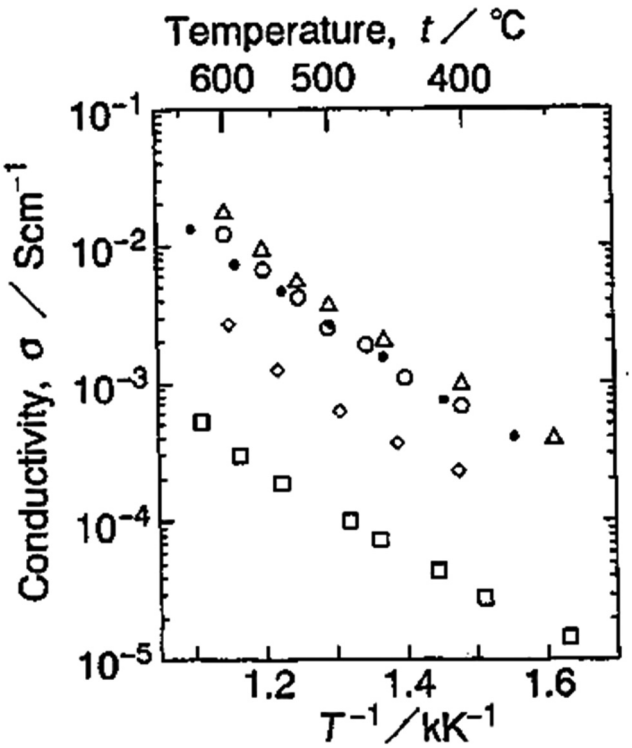

Fig. 22 Arrhenius plots of conductivity of $LiBaF_{3-x}H_x$ in H_2: □$x = 0$, ◊$x = 0.05$, ○$x = 0.1$, Δ$x = 0.2$, ● $LiBa_{0.9}K_{0.1}F_{2.8}H_{0.1}$.[106]

possibility of developing solid electrochemical devices based on H^- conductors. Although recent studies have shown the possibility of ambient pressure synthesis of oxyhydrides, the requirement for high pressure in synthesizing the desired oxyhydrides and the lack of stability study are major obstacles for practical applications of oxyhydrides.

5.3 Nitrohydrides and hydrofluorides

Like oxyhydrides, H^- diffusion was also observed in nitrohydrides such as Ba_2NH,[101,102] Sr_2NH,[103] and Sr_2LiH_2N.[104] Studies have discovered that these nitrohydrides exhibit layered structures at high concentrations (up to 15%) of H-vacancies, which favors H^- diffusion. The H^- migration proceeds in the planes occupied by H^-, in uncorrelated jumps between regular lattice sites, see Fig. 21(a). The high and pure mobility of H^- gives rise to the high conductivity of 1 S cm^{-1} above certain temperatures (*e.g.* 525 K for Ba_2NH), see Fig. 21(b). However, there is a lack of systematic study on the origin of such high conductivity, leaving nitrohydrides group wide open for further investigations.

Hydrofluorides, for example, $CaF_{2-x}H_x$,[105] and $LiBaF_{3-x}H_x$,[106] have a perovskite structure, in which ionic radii of H^- and F^- are similar (r_{H^-} = 2.08 Å, r_{F^-} = 1.33 Å). EMF measurements reveal the high conductivity of $LiBaF_{3-x}H_x$ in H_2 atmosphere, varying from 10^{-5}–10^{-2} S cm^{-1} at temperatures of 330–650 °C, see Fig. 22. However, such hydride compounds are subject to oxidation

Table 1 Representative H^+/H^- conductors and their corresponding conductivities and optimal operating conditions

Material	Conductivity (S cm^{-1})	Optimal operating conditions	Ref.
Oxides as H^+ conductors			
Perovskites			
$BaCe_{0.9}Y_{0.1}O_{3-\delta}$ (BCY)	1.8×10^{-2}–7×10^{-2} at 600–1000 °C	500–750 °C	27
$BaZr_{0.9}Y_{0.1}O_{3-\delta}$ (BZY)	1.6×10^{-3}–6×10^{-3} at 600–1000 °C	500–750 °C	28
$BaZr_{0.1}Ce_{0.7}Y_{0.1}Yb_{0.1}O_{3-\delta}$ (BZCYYb)	5×10^{-3}–5×10^{-2} at 400–750 °C	500–750 °C	23
RP oxides			
$BaLaIn_{0.9}Ti_{0.1}O_{4.05}$	7.4×10^{-8}–2.6×10^{-6} at 250–450 °C		39
Pyrochlores oxides			
$(La_{1.95}Ca_{0.05})Zr_2O_{7-\delta}$	6.3×10^{-5}–1.1×10^{-3} at 400–900 °C	500–800 °C	41
Rare-earth *ortho*-niobates and *ortho*-tantalates			
1% Ca-doped $LaNbO_4$	2×10^{-5}–9×10^{-4} at 400–1000 °C	700–1000 °C	45
Perovskites with MC			
BZY-$(Li_{0.62}K_{0.38})_2CO_3$	0.01–0.78 at 400–660 °C	500–650 °C	33
Solid polyanionic compounds as H^+ conductors			
Phosphates/pyrophosphates			
1 mol% Sr-doped $LaPO_4$	8.7×10^{-6}–2.6×10^{-4} at 500–930 °C	500–900 °C	56
1 mol% Sr-doped $CePO_4$	8.8×10^{-6}–3.8×10^{-4} at 500–930 °C	500–900 °C	56
$Sn_{0.9}In_{0.1}P_2O_7$	7.1×10^{-2}–1.8×10^{-1} at 75–300 °C	200–300 °C	65
$CsHSO_4$	1.6×10^{-7}–3.5×10^{-2} at 100–190 °C	140–190 °C	55
$Rb_3H(SeO_4)_2$	9.6×10^{-8}–8.3×10^{-3} at 75–235 °C	180–235 °C	55
CsH_2PO_4	3.1×10^{-6}–2.71×10^{-2} at 155–252 °C	200–250 °C, $pH_2O \geq 0.4$ atm	68
Sulphates and nitrates			
Li_2SO_4-45 mol%Al_2O_3	3.2×10^{-5}–1.8×10^{-2} at 350–600 °C	450–600 °C	50
$RbNO_3$–Al_2O_3	2×10^{-4}–6.6×10^{-2} at 325–650 °C	500–650 °C	52 and 53
$CsNO_3$–Al_2O_3	1.9×10^{-4}–9.4×10^{-2} at 400–650 °C	550–650 °C	52 and 53
Hydrates as H^+ conductors			
Mesoporous nanocomposites			
TiO_2–P_2O_5	6×10^{-3}–1.5×10^{-2} at 50–200 °C	50–200 °C, 100%RH	72
40% SO_3H-MCM-41	1×10^{-3}–2×10^{-2} at 60–140 °C	60–140 °C, 100%RH	74
Heteropolyacid hydrates			
$H_4SiW_{12}O_{40}{\cdot}28H_2O$	2×10^{-2} at 25 °C	<100 °C, >70%RH	77
$H_3PW_{12}O_{40}{\cdot}29H_2O$	8×10^{-2} at 25 °C	<100 °C, >70%RH	78
$H_3PMo_{12}O_{40}{\cdot}29H_2O$	1.7×10^{-1} at 25 °C	<100 °C, >70%RH	79
Layered hydrates			
$HUO_2PO_4{\cdot}4H_2O$	5×10^{-3} at 25 °C	<100 °C, high RH	82
Oxide hydrates			
$V_2O_5{\cdot}nH_2O$, $ZrO_2{\cdot}nH_2O$	1×10^{-2} at 25 °C	<150 °C, 100%RH	89
H^- conductors			
Hydrides			
BaH_2	5.4×10^{-6}–1.68×10^{-1} at 100–630 °C	470–630 °C	92
$Sr_{0.925}Na_{0.075}LiH_{2.925}$	5.0×10^{-6} at 25 °C	25–150 °C	94
Perovskite oxyhydrides			
$La_2Sr_{0.1}LiH_{0.9}O_3$	3.86×10^{-7}–2.04×10^{-5} at 200–300 °C	200–300 °C	95
$Ba_{1.75}LiH_{2.7}O_{0.9}$	2.24×10^{-7}–1.38×10^{-2} at 210–350 °C	300–350 °C	98
$LaH_{1.92}O_{0.54}$	9.24×10^{-10}–2.6×10^{-2} at 85–342 °C	250–342 °C	100
Nitrohydrides and hydrofluorides			
Ba_2NH	3.5×10^{-6}–1.1 at 35–435 °C	350–400 °C	101
$LiBaF_{2.8}H_{0.2}$	4×10^{-4}–1.7×10^{-2} at 350–600 °C	350–600 °C	106

and thus suffered stability issues, making them difficult in applications.

6. Summary

In summary, the most investigated H^+ and H^- conductors have been reviewed in this article in terms of structures, conduction mechanisms, conductivities, and optimal conducting conditions. The representative conductors for each class are summarized in Table 1.

Overall, despite some results shown in electrochemical cells and H_2 separation membranes, no industrial scale devices have been demonstrated for proton and hydride-anion conductors. The main challenges for H^+/H^- based electrochemical cells to be practical are poor chemical, thermal and mechanical stabilities, difficulty to process and chemical reactivity under operating conditions. To advance H^+/H^- based electrochemical cells, further scientific studies and engineering efforts are greatly needed.

Conflicts of interest

There are no conflicts to declare.

Acknowledgements

We would like to thank the National Science Foundation for the financial support under award number 1801284 and the Department of Energy, Office Fossil Fuels, National Energy Technology Laboratory for the financial support under award number DE-FE-0032111.

References

1 P. F. Lang and C. S. Barry, Ionic radii for Group 1 and Group 2 halide, hydride, fluoride, oxide, sulfide, selenide and telluride crystals, *Dalton Trans.*, 2010, **39**(33), 7786–7791, DOI: 10.1039/C0DT00401D.

2 L. Malavasi, M. Karlsson and M. Coduri, Structure-Property Correlation in Oxide-Ion and Proton Conductors for Clean Energy Applications: Recent Experimental and Computational Advancements, *J. Mater. Chem. A*, 2022, DOI: 10.1039/D1TA10326A.

3 C. Duan, J. Huang, N. Sullivan and R. O'Hayre, Proton-conducting oxides for energy conversion and storage, *Appl. Phys. Rev.*, 2020, 7(1), 011314, DOI: 10.1063/1.5135319.

4 K.-D. Kreuer, Proton-conducting oxides, *Annu. Rev. Mater. Res.*, 2003, **33**(1), 333–359, DOI: 10.1146/annurev.matsci.33.022802.091825.

5 H. Iwahara, Proton conducting ceramics and their applications, *Solid State Ionics*, 1996, **86**, 9–15, DOI: 10.1016/0167-2738(96)00087-2.

6 N. Danilov, A. Tarutin, J. Lyagaeva, G. Vdovin and D. Medvedev, CO_2-promoted hydrogen production in a protonic ceramic electrolysis cell, *J. Mater. Chem. A*, 2018, **6**(34), 16341–16346, DOI: 10.1039/C8TA05820B.

7 S. Rajendran, N. K. Thangavel, H. Ding, Y. Ding, D. Ding and L. M. R. Arava, Tri-doped $BaCeO_3$–$BaZrO_3$ as a chemically stable electrolyte with high proton-conductivity for intermediate temperature solid oxide electrolysis cells (SOECs), *ACS Appl. Mater. Interfaces*, 2020, **12**(34), 38275–38284, DOI: 10.1021/acsami.0c12532.

8 R. Murphy, Y. Zhou, L. Zhang, L. Soule, W. Zhang, Y. Chen and M. Liu, A new family of proton-conducting electrolytes for reversible solid oxide cells: $BaHfxCe_{0.8-x}Y_{0\ 1}Yb_{0.1}O_{3-\delta}$, *Adv. Funct. Mater.*, 2020, **30**(35), 2002265, DOI: 10.1002/adfm.202002265.

9 A. P. Tarutin, M. Yu Gorshkov, I. N. Bainov, G. K. Vdovin, A. I. Vylkov, J. G. Lyagaeva and D. A. Medvedev, Barium-doped nickelates $Nd_{2-x}Ba_xNiO_{4+\delta}$ as promising electrode materials for protonic ceramic electrochemical cells, *Ceram. Int.*, 2020, **46**(15), 24355–24364, DOI: 10.1016/j.ceramint.2020.06.217.

10 M. Sakbodin, E. Schulman, S. Cheng, Y.-L. Huang, Y. Pan, P. Albertus, E. D. Wachsman and D. Liu, Direct Nonoxidative Methane Conversion in an Autothermal Hydrogen-Permeable Membrane Reactor, *Adv. Energy Mater.*, 2021, **11**(46), 2102782, DOI: 10.1002/aenm.202102782.

11 G. Ma, F. Zhang, J. Zhu and G. Meng, Proton conduction in $La_{0.9}Sr_{0.1}Ga_{0.8}Mg_{0.2}O_{3-\alpha}$, *Chem. Mater.*, 2006, **18**(25), 6006–6011, DOI: 10.1021/cm0612954.

12 N. Xu, C. Zhang and K. Huang, Proton-mediated energy storage in intermediate-temperature solid-oxide metal–air batteries, *J. Mater. Chem. A*, 2018, **6**(42), 20659–20662, DOI: 10.1039/C8TA08180H.

13 C. J. Bartel, C. Sutton, B. R. Goldsmith, R. Ouyang, C. B. Musgrave, L. M. Ghiringhelli and M. Scheffler, New tolerance factor to predict the stability of perovskite oxides and halides, *Sci. Adv.*, 2019, **5**(2), eaav0693, DOI: 10.1126/sciadv.aav0693.

14 M. Papac, V. Stevanović, A. Zakutayev and R. O'Hayre, Triple ionic–electronic conducting oxides for next-generation electrochemical devices, *Nat. Mater.*, 2021, **20**(3), 301–313, DOI: 10.1038/s41563-020-00854-8.

15 H. Wang, X. Wang, B. Meng, X. Tan, K. S. Loh, J. Sunarso and S. Liu, Perovskite-based mixed protonic–electronic conducting membranes for hydrogen separation: recent status and advances, *J. Ind. Eng. Chem.*, 2018, **60**, 297–306, DOI: 10.1016/j.jiec.2017.11.016.

16 M. Ni and Z. Shao, Fuel cells that operate at 300 to 500 C, *Science*, 2020, **369**(6500), 138–139, DOI: 10.1126/science.abc9136.

17 H. Su and Y. H. Hu, Degradation issues and stabilization strategies of protonic ceramic electrolysis cells for steam electrolysis, *Energy Sci. Eng.*, 2022, **10**(5), 1706–1725, DOI: 10.1002/ese3.1010.

18 W. Wang, D. Medvedev and Z. Shao, Gas humidification impact on the properties and performance of perovskite-type functional materials in proton-conducting solid oxide cells, *Adv. Funct. Mater.*, 2018, **28**(48), 1802592, DOI: 10.1002/adfm.201802592.

19 H. Iwahara, T. Esaka, H. Uchida and N. Maeda, Proton conduction in sintered oxides and its application to steam electrolysis for hydrogen production, *Solid State Ionics*, 1981, **3**, 359–363, DOI: 10.1016/0167-2738(81)90113-2.

20 H. Uchida, N. Maeda and H. Iwahara, Relation between proton and hole conduction in $SrCeO_3$-based solid electrolytes under water-containing atmospheres at high temperatures, *Solid State Ionics*, 1983, **11**(2), 117–124, DOI: 10.1016/0167-2738(83)90048-6.

21 K.-D. Kreuer, W. Münch, A. Fuchs, U. Klock and J. Maier, Proton conducting alkaline earth zirconates and titanates for high drain electrochemical applications, *Solid State Ionics*, 2001, **145**(1–4), 295–306, DOI: 10.1016/S0167-2738(01)00953-5.

22 C. Duan, R. Kee, H. Zhu, N. Sullivan, L. Zhu, L. Bian, D. Jennings and R. O'Hayre, Highly efficient reversible protonic ceramic electrochemical cells for power generation and fuel production, *Nat. Energy*, 2019, **4**(3), 230–240, DOI: 10.1038/s41560-019-0333-2.

23 L. Yang, S. Wang, K. Blinn, M. Liu, Z. Liu, Z. Cheng and M. Liu, Enhanced sulfur and coking tolerance of a mixed ion conductor for SOFCs: $BaZr_{0.1}Ce_{0.7}Y_{0.2-x}Yb_xO_{3-\delta}$, *Science*, 2009, **326**(5949), 126–129, DOI: 10.1126/science.1174811.

24 S. Choi, J. K. Chris, Y. Liang, X. Zhang, I. Takeuchi, H.-I. Ji and S. M. Haile, Exceptional power density and stability at intermediate temperatures in protonic ceramic fuel cells, *Nat. Energy*, 2018, **3**(3), 202–210, DOI: 10.1038/s41560-017-0085-9.

25 L. Bi, P. S. Shahid and E. Traversa, Y-doped $BaZrO_3$ as a chemically stable electrolyte for proton-conducting solid oxide electrolysis cells (SOECs), *J. Mater. Chem. A*, 2015, **3**(11), 5815–5819, DOI: 10.1039/C4TA07202B.

26 G. C. Mather and M. S. Islam, Defect and dopant properties of the $SrCeO_3$-based proton conductor, *Chem. Mater.*, 2005, **17**(7), 1736–1744, DOI: 10.1021/cm047976l.

27 Y. Yoo and N. Lim, Performance and stability of proton conducting solid oxide fuel cells based on yttrium-doped barium cerate-zirconate thin-film electrolyte, *J. Power Sources*, 2013, **229**, 48–57, DOI: 10.1016/j.jpowsour.2012.11.094.

28 C. Y. R. Vera, H. Ding, D. Peterson, W. T. Gibbons, M. Zhou and D. Ding, A mini-review on proton conduction of $BaZrO_3$-based perovskite electrolytes, *J. Phys.: Energy*, 2021, **3**(3), 032019, DOI: 10.1088/2515-7655/ac12ab.

29 S. Barison, M. Battagliarin, S. Boldrini, G. Chiodelli and L. Doubova, Monica Fabrizio, Rosalba Gerbasi, and Lorenzo Malavasi. $BaCe_{1-x-y}Zr_xY_yO_{3-d}$ Proton Conductors: The Role of the Synthetic Route on their Properties, *ECS Trans.*, 2008, **11**(33), 89, DOI: 10.1149/1.3038912.

30 S. Barison, M. Battagliarin, T. Cavallin and L. Doubova, Monica Fabrizio, Cecilia Mortalo, Stefano Boldrini, Lorenzo Malavasi, and Rosalba Gerbasi. High conductivity and chemical stability of $BaCe_{1-x-y}Zr_xY_yO_{3-\delta}$ proton conductors prepared by a sol–gel method, *J. Mater. Chem.*, 2008, **18**(42), 5120–5128, DOI: 10.1039/B808344D.

31 S. Choi, C. D. Timothy and M. H. Sossina, Protonic ceramic electrochemical cells for hydrogen production and electricity generation: exceptional reversibility, stability, and demonstrated faradaic efficiency, *Energy Environ. Sci.*, 2019, **12**(1), 206–215, DOI: 10.1039/C8EE02865F.

32 X. Li, N. Xu, L. Zhang and K. Huang, Combining proton conductor $BaZr_{0.8}Y_{0.2}O_{3-\delta}$ with carbonate: Promoted densification and enhanced proton conductivity, *Electrochem. Commun.*, 2011, **13**(7), 694–697, DOI: 10.1016/j.elecom.2011.04.012.

33 X. Lei, K. Huang and C. Qin, Enhanced interfacial proton migration on BaZr (Y) O3 by molten carbonate: a first principles study, *Solid State Ionics*, 2016, **289**, 48–54, DOI: 10.1016/j.ssi.2016.02.018.

34 X. Lei, C. Qin and K. Huang, Energetics of proton transfer in alkali carbonates: a first principles calculation, *RSC Adv.*, 2015, **5**(69), 56205–56209, DOI: 10.1039/C5RA07975F.

35 G. Nirala, D. Yadav and S. Upadhyay, Ruddlesden–Popper phase A_2BO_4 oxides: Recent studies on structure, electrical, dielectric, and optical properties, *J. Adv. Ceram.*, 2020, **9**(2), 129–148, DOI: 10.1007/s40145-020-0365-x.

36 A. P. Tarutin, G. L. Julia, D. A. Medvedev, L. Bi and A. A. Yaremchenko, Recent advances in layered $Ln_2NiO_{4+\delta}$ nickelates: Fundamentals and prospects of their applications in protonic ceramic fuel and electrolysis cells, *J. Mater. Chem. A*, 2021, **9**(1), 154–195, DOI: 10.1039/D0TA08132A.

37 W. Li, B. Guan, L. Ma, S. Hu, N. Zhang and X. Liu, High performing triple-conductive $Pr_2NiO_{4+\delta}$ anode for proton-conducting steam solid oxide electrolysis cell, *J. Mater. Chem. A*, 2018, **6**(37), 18057–18066, DOI: 10.1039/C8TA04018D.

38 S. Upasen, P. Batocchi, F. Mauvy, A. Slodczyk and P. Colomban, Protonation and structural/chemical stability of $Ln_2NiO_{4+\delta}$ ceramics *vs.* H_2O/CO_2: High temperature/water pressure ageing tests, *J. Alloys Compd.*, 2015, **622**, 1074–1085, DOI: 10.1016/j.jallcom.2014.11.017.

39 N. Tarasova, I. Animitsa, A. Galisheva and V. Pryakhina, Protonic transport in the new phases $BaLaIn_{0.9}M_{0.1}O_{4.05}$ (M = Ti, Zr) with Ruddlesden–Popper structure, *Solid State Sci.*, 2020, **101**, 106121, DOI: 10.1016/j.solidstatesciences.2020.106121.

40 H. Yamamura, H. Nishino and K. Kakinuma, Ac conductivity for $Eu_2Zr_2O_7$ and $La_2Ce_2O_7$ with pyrochlore-type composition, *J. Ceram. Soc. Jpn.*, 2004, **112**(10), 553–558, DOI: 10.2109/jcersj.112.553.

41 T. Omata, K. Okuda, S. Tsugimoto and S. Otsuka-Matsuo-Yao, Water and hydrogen evolution properties and protonic conducting behaviors of Ca^{2+}-doped $La_2Zr_2O_7$ with a pyrochlore structure, *Solid State Ionics*, 1997, **104**(3–4), 249–258, DOI: 10.1016/S0167-2738(97)00433-5.

42 T. Shimura, M. Komori and H. Iwahara, Ionic conduction in pyrochlore-type oxides containing rare earth elements at high temperature, *Solid State Ionics*, 1996, **86**, 685–689, DOI: 10.1016/0167-2738(96)00148-8.

43 T. Omata and S. Otsuka-Yao-Matsuo, Electrical properties of proton-conducting Ca^{2+}-doped $La_2Zr_2O_7$ with a

pyrochlore-type structure, *J. Electrochem. Soc.*, 2001, **148**(6), E252, DOI: 10.1149/1.1369370.

44 M. E. Björketun, S. K. Christopher, B. J. Nyman and G. Wahnström, Protonic defects in pure and doped $La_2Zr_2O_7$ pyrochlore oxide, *Solid State Ionics*, 2008, **178**(31–32), 1642–1647, DOI: 10.1016/j.ssi.2007.10.014.

45 R. Haugsrud and T. Norby, Proton conduction in rare-earth *ortho*-niobates and *ortho*-tantalates, *Nat. Mater.*, 2006, **5**(3), 193–196, DOI: 10.1038/nmat1591.

46 K. D. Kreuer, On the complexity of proton conduction phenomena, *Solid State Ionics*, 2000, **136**, 149–160, DOI: 10.1016/S0167-2738(00)00301-5.

47 H. Fjeld, K. Toyoura, R. Haugsrud and T. Norby, Proton mobility through a second order phase transition: theoretical and experimental study of $LaNbO_4$, *Phys. Chem. Chem. Phys.*, 2010, **12**(35), 10313–10319, DOI: 10.1039/C002851G.

48 B. Heed, B. Zhu, B.-E. Mellander and A. Lundén, Proton conductivity in fuel cells with solid sulphate electrolytes, *Solid State Ionics*, 1991, **46**(1–2), 121–125, DOI: 10.1016/0167-2738(91)90139-3.

49 B. Zhu and B.-E. Mellander, Intermediate temperature fuel cells with electrolytes based on oxyacid salts, *J. Power Sources*, 1994, **52**(2), 289–293, DOI: 10.1016/0378-7753(94)02145-7.

50 B. Zhu and B.-E. Mellander, Novel proton conducting ceramics for solid state fuel cells, *ECS Proceedings Volumes 1993*, 1993, vol. 1, p. 156, DOI: 10.1149/199304.0156PV.

51 B. Zhu, Z. H. Lai and B.-E. Mellander, Structure and ionic conductivity of lithium sulphate–aluminum oxide ceramics, *Solid State Ionics*, 1994, **70**, 125–129, DOI: 10.1016/0167-2738(94)90296-8.

52 B. Zhu and B.-E. Mellander, Proton conduction in nitrate-based oxides and related ceramics at intermediate temperatures, *Solid State Ionics*, 1994, **70**, 285–290, DOI: 10.1016/0167-2738(94)90324-7.

53 B. Zhu and B.-E. Mellander, Proton conduction in salt-ceramic composite systems, *Solid State Ionics*, 1995, **77**, 244–249, DOI: 10.1016/0167-2738(94)00275-W.

54 N. F. Uvarov, P. Vaněk, Y. I. Yuzyuk, V. Železný, V. Studnička, B. B. Bokhonov, V. E. Dulepov and J. Petzelt, Properties of rubidium nitrate in ion-conducting $RbNO_3$–Al_2O_3 nanocomposites, *Solid State Ionics*, 1996, **90**(1–4), 201–207, DOI: 10.1016/S0167-2738(96)00400-6.

55 S. M. Haile, A. B. Dane, C. R. I. Chisholm and R. B. Merle, Solid acids as fuel cell electrolytes, *Nature*, 2001, **410**(6831), 910–913, DOI: 10.1038/35073536.

56 N. Kitamura, K. Amezawa, Y. Tomii, T. Hanada, N. Yamamoto, T. Omata and S. Otsuka-Yao-Matsuo, Electrical conduction properties of Sr-doped $LaPO_4$ and $CePO_4$ under oxidizing and reducing conditions, *J. Electrochem. Soc.*, 2005, **152**(4), A658, DOI: 10.1149/1.1861993.

57 T. Norby and N. Christiansen, Proton conduction in Ca- and Sr-substituted $LaPO_4$, *Solid State Ionics*, 1995, **77**, 240–243, DOI: 10.1016/0167-2738(94)00274-V.

58 K. Amezawa, H. Maekawa, Y. Tomii and N. Yamamoto, Protonic conduction and defect structures in Sr-doped $LaPO_4$, *Solid State Ionics*, 2001, **145**(1–4), 233–240, DOI: 10.1016/S0167-2738(01)00963-8.

59 S. Gallini, M. Hänsel, T. Norby, M. T. Colomer and J. R. Jurado, Impedance spectroscopy and proton transport number measurements on Sr-substituted $LaPO_4$ prepared by combustion synthesis, *Solid State Ionics*, 2003, **162**, 167–173, DOI: 10.1016/S0167-2738(03)00220-0.

60 N. Kitamura, K. Amezawa, Y. Tomii and N. Yamamoto, Protonic conduction in rare earth orthophosphates with the monazite structure, *Solid State Ionics*, 2003, **162**, 161–165, DOI: 10.1016/S0167-2738(03)00219-4.

61 G. Alberti, M. Casciola, S. Cavalaglio and R. Vivani, Proton conductivity of mesoporous zirconium phosphate pyrophosphate, *Solid State Ionics*, 1999, **125**(1–4), 91–97, DOI: 10.1016/S0167-2738(99)00162-9.

62 M. Nagao, T. Kamiya, P. Heo, A. Tomita, T. Hibino and M. Sano, Proton conduction in In^{3+}-doped SnP_2O^7 at intermediate temperatures, *J. Electrochem. Soc.*, 2006, **153**(8), A1604, DOI: 10.1149/1.2210669.

63 Y. Li, T. Kunitake, Y. Aoki and E. Muto, Efficient, anhydrous proton-conducting nanofilms of Y-doped zirconium pyrophosphate at intermediate temperatures, *Adv. Mater.*, 2008, **20**(12), 2398–2404, DOI: 10.1016/j.ssi.2008.01.046.

64 X. Sun, S. Wang, Z. Wang, X. Ye, T. Wen and F. Huang, Proton conductivity of CeP_2O_7 for intermediate temperature fuel cells, *Solid State Ionics*, 2008, **179**(21–26), 1138–1141, DOI: 10.1016/j.ssi.2008.01.046.

65 M. Nagao, T. Kamiya, P. Heo, A. Tomita, T. Hibino and M. Sano, Proton conduction in In^{3+}-doped SnP_2O_7 at intermediate temperatures, *J. Electrochem. Soc.*, 2006, **153**(8), A1604, DOI: 10.1149/1.2210669.

66 S.-H. Lee, S.-T. Lee, D.-H. Lee, S.-M. Lee, S.-S. Han and S.-K. Lim, $CsHSO_4$/TiP_2O_7 composite membrane for high temperature (>150 °C) proton exchange membrane fuel cells, *Int. J. Hydrogen Energy*, 2015, **40**(37), 12770–12775, DOI: 10.1016/j.ijhydene.2015.07.128.

67 T. Hibino, K. Kobayashi, M. Nagao and S. Kawasaki, High-temperature supercapacitor with a proton-conducting metal pyrophosphate electrolyte, *Sci. Rep.*, 2015, **5**(1), 1–7, DOI: 10.1038/srep07903.

68 A. I. Baranov, B. V. Merinov, A. V. Tregubchenko, V. P. Khiznichenko, L. A. Shuvalov and N. M. Schagina, Fast proton transport in crystals with a dynamically disordered hydrogen bond network, *Solid State Ionics*, 1989, **36**(3–4), 279–282, DOI: 10.1039/B604311A.

69 S. M. Haile, R. I. C. Calum, K. Sasaki, D. A. Boysen and T. Uda, Solid acid proton conductors: from laboratory curiosities to fuel cell electrolytes, *Faraday Discuss.*, 2007, **134**, 17–39, DOI: 10.1039/B604311A.

70 A. Ishikawa, H. Maekawa, T. Yamamura, Y. Kawakita, K. Shibata and M. Kawai, Proton dynamics of CsH_2PO_4 studied by quasi-elastic neutron scattering and PFG-NMR, *Solid State Ionics*, 2008, **179**(40), 2345–2349, DOI: 10.1016/j.ssi.2008.10.002.

71 V. G. Ponomareva, A. K. Konstantin, R. D. Gus'kov, I. N. Bagryantseva, N. F. Uvarov and V. P. Fedin, Proton

conducting hybrid compounds based on $CsH_5(PO_4)_2$ metal–organic coordination frameworks, *Solid State Ionics*, 2019, **343**, 115084, DOI: 10.1016/j.ssi.2019.115084.

72 M. Yamada, D. Li, I. Honma and H. Zhou, A self-ordered, crystalline glass, mesoporous nanocomposite with high proton conductivity of 2×10^{-2} S cm^{-1} at intermediate temperature, *J. Am. Chem. Soc.*, 2005, **127**(38), 13092–13093, DOI: 10.1021/ja052914x.

73 M. Nogami, H. Matsushita, Y. Goto and T. Kasuga, A Sol–Gel-Derived Glass as a Fuel Cell Electrolyte, *Adv. Mater.*, 2000, **12**(18), 1370–1372, DOI: 10.1002/1521-4095(200009)12:18<1370::AID-ADMA1370>3.0.CO;2-1.

74 R. Marschall, J. Rathouský and M. Wark, Ordered functionalized silica materials with high proton conductivity, *Chem. Mater.*, 2007, **19**(26), 6401–6407, DOI: 10.1021/cm071164i.

75 P. Choi, H. J. Nikhil, T. M. Thampan and R. Datta, Consideration of thermodynamic, transport, and mechanical properties in the design of polymer electrolyte membranes for higher temperature fuel cell operation, *J. Polym. Sci., Part B: Polym. Phys.*, 2006, **44**(16), 2183–2200, DOI: 10.1002/polb.20858.

76 M. Vinothkannan, A. R. Kim, S. Ramakrishnan, Y.-T. Yu and D. J. Yoo, Advanced Nafion nanocomposite membrane embedded with unzipped and functionalized graphite nanofibers for high-temperature hydrogen-air fuel cell system: The impact of filler on power density, chemical durability and hydrogen permeability of membrane, *Composites, Part B*, 2021, **215**, 108828, DOI: 10.1016/j.compositesb.2021.108828.

77 O. Nakamura, I. Ogino and T. Kodama, Temperature and humidity ranges of some hydrates of high-proton-conductive dodecamolybdophosphoric acid and dodecatungstophosphoric acid crystals under an atmosphere of hydrogen or either oxygen or air, *Solid State Ionics*, 1981, **3**, 347–351, DOI: 10.1016/0167-2738(81)90111-9.

78 K.-D. Kreuer, Fast proton transport in solids, *J. Mol. Struct.*, 1988, **177**, 265–276, DOI: 10.1016/0022-2860(88)80093-0.

79 O. Nakamura, T. Kodama, I. Ogino and Y. Miyake, High-conductivity solid proton conductors: Dodecamolybdophosphoric acid and dodecatungstophosphoric acid crystals, *Chem. Lett.*, 1979, (1), 17–18, DOI: 10.1246/cl.1979.17.

80 U. B. Mioč, K. M. Slobodan, D. Malović, V. Stamenković, P. Colomban, M. M. Mitrović and R. Dimitrijević., Structure and proton conductivity of 12-tungstophosphoric acid doped silica, *Solid State Ionics*, 1997, **97**(1–4), 239–246, DOI: 10.1016/S0167-2738(97)00089-1.

81 N. Lakshmi and S. Chandra, Proton conducting composites of heteropolyacid hydrates (phosphomolybdic and phosphotungstic acids) dispersed with insulating Al_2O_3, *Phys. Status Solidi A*, 2001, **186**(3), 383–399, DOI: 10.1002/1521-396X(200108)186:3<383::AID-PSSA383>3.0.CO;2-9.

82 A. T. Howe and G. S. Mark, Studies of layered uranium(VI) compounds. I. High proton conductivity in polycrystalline hydrogen uranyl phosphate tetrahydrate, *J. Solid State Chem.*, 1979, **28**(3), 345–361, DOI: 10.1016/0022-4596(79)90085-9.

83 G. Alberti, M. Casciola, U. Costantino, A. Peraio and T. Rega, Proton-conducting solid dispersions of silica and zirconium phosphate pyrophosphate, *J. Mater. Chem.*, 1995, **5**(11), 1809–1812, DOI: 10.1039/JM9950501809.

84 G. Alberti and M. Casciola, Layered metalIV phosphonates, a large class of inorgano-organic proton conductors, *Solid State Ionics*, 1997, **97**(1–4), 177–186, DOI: 10.1016/S0167-2738(97)00070-2.

85 G. Alberti, L. Boccali, M. Casciola, L. Massinelli and E. Montoneri, Protonic conductivity of layered zirconium phosphonates containing—SO_3H groups. III. Preparation and characterization of γ-zirconium sulfoaryl phosphonates, *Solid State Ionics*, 1996, **84**(1–2), 97–104, DOI: 10.1016/S0167-2738(96)83011-6.

86 M. G. Shilton and T. H. Arthur, Rapid H^+ conductivity in hydrogen uranyl phosphate-A solid H^+ electrolyte, *Mater. Res. Bull.*, 1977, **12**(7), 701–706, DOI: 10.1016/0025-5408(77)90129-5.

87 N. Miura and N. Yamazoe, Development of new chemical sensors based on low-temperature proton conductors, *Solid State Ionics*, 1992, **53**, 975–982, DOI: 10.1016/0167-2738(92)90279-X.

88 Y.-M. Li, M. Hibino, M. Miyayama and T. Kudo, Proton Conductivity of Some Hydrated Compounds at Intermediate Temperature up to 150 °C under High Water Vapor Pressure, *Electrochemistry*, 2001, **69**(1), 2–5, DOI: 10.5796/electrochemistry.69.2.

89 K. Zhu, T. Wu, S. Sun, W. van den Bergh, M. Stefik and K. Huang, Synergistic H^+/Zn^{2+} dual ion insertion mechanism in high-capacity and ultra-stable hydrated VO_2 cathode for aqueous Zn-ion batteries, *Energy Storage Mater.*, 2020, **29**, 60–70, DOI: 10.1016/j.ensm.2020.03.030.

90 M. C. Verbraeken, E. Suard and J. T. S. Irvine, Structural and electrical properties of calcium and strontium hydrides, *J. Mater. Chem.*, 2009, **19**(18), 2766–2770, DOI: 10.1039/B820173K.

91 B. Zhu and X. Liu, LiF–CaH_2 alumina electrolytes for intermediate temperature fuel cell applications, *Electrochem. Commun.*, 2000, **2**(1), 10–14, DOI: 10.1016/S1388-2481(99)00139-3.

92 M. C. Verbraeken, C. Cheung, E. Suard and J. T. S. Irvine, High H^- ionic conductivity in barium hydride, *Nat. Mater.*, 2015, **14**(1), 95–100, DOI: 10.1038/nmat4136.

93 H. Ubukata, F. Takeiri, K. Shitara, C. Tassel, T. Saito, T. Kamiyama, T. Broux, A. Kuwabara, G. Kobayashi and H. Kageyama, Anion ordering enables fast H^- conduction at low temperatures, *Sci. Adv.*, 2021, **7**(23), eabf7883, DOI: 10.1126/sciadv.abf7883.

94 T. Hirose, T. Mishina, N. Matsui, K. Suzuki, T. Saito, T. Kamiyama, M. Hirayama and R. Kanno, Fast Hydride-Ion Conduction in Perovskite Hydrides AE LiH_3, *ACS Appl. Energy Mater.*, 2022, **5**(3), 2968–2974, DOI: 10.1021/acsaem.1c03633.

95 G. Kobayashi, Y. Hinuma, S. Matsuoka, A. Watanabe, M. Iqbal, M. Hirayama, M. Yonemura, T. Kamiyama, I. Tanaka and R. Kanno, Pure H-conduction in oxyhydrides, *Science*, 2016, **351**(6279), 1314–1317, DOI: 10.1126/science.aac9185.

96 F. Takeiri, A. Watanabe, A. Kuwabara, H. Nawaz, N. I. P. Ayu, M. Yonemura, R. Kanno and G. Kobayashi, Ba_2ScHO_3: H-conductive layered oxyhydride with H-site selectivity, *Inorg. Chem.*, 2019, **58**(7), 4431–4436, DOI: **10.1021/acs.inorgchem.8b03593**.

97 C. A. Bridges, F. Fernandez-Alonso, J. P. Goff and M. J. Rosseinsky, Observation of Hydride Mobility in the Transition-Metal Oxide Hydride $LaSrCoO_3HO_7$, *Adv. Mater.*, 2006, **18**(24), 3304–3308, DOI: **10.1002/adma.200601266**.

98 F. Takeiri, A. Watanabe, K. Okamoto, D. Bresser, S. Lyonnard, B. Frick and A. Ali, *et al.*, Hydride-ion-conducting K_2NiF_4-type Ba–Li oxyhydride solid electrolyte, *Nat. Mater.*, 2022, **21**(3), 325–330, DOI: **10.1038/s41563-021-01175-0**.

99 Y. Kobayashi, O. J. Hernandez, T. Sakaguchi, T. Yajima, T. Roisnel, Y. Tsujimoto and M. Morita, *et al.*, An oxyhydride of $BaTiO_3$ exhibiting hydride exchange and electronic conductivity, *Nat. Mater.*, 2012, **11**(6), 507–511, DOI: **10.1038/nmat3302**.

100 K. Fukui, S. Iimura, T. Tada, S. Fujitsu, M. Sasase, H. Tamatsukuri, T. Honda, K. Ikeda, T. Otomo and H. Hosono, Characteristic fast H^- ion conduction in oxygen-substituted lanthanum hydride, *Nat. Commun.*, 2019, **10**(1), 1–8, DOI: **10.1038/s41467-019-10492-7**.

101 F. Altorfer, W. Bührer, B. Winkler, G. Coddens, R. Essmann and H. Jacobs, H-jump diffusion in barium-nitride-hydride Ba_2NH, *Solid State Ionics*, 1994, **70**, 272–277, DOI: **10.1016/0167-2738(94)90322-0**.

102 B. Wegner, R. Essmann, J. Bock, H. Jacobs and P. Fischer, Structure and H-ionic-conductivity of barium hydride nitride, Ba_2H (D) N, *Eur. J. Solid State Inorg. Chem.*, 1992, **29**(6), 1217–1227.

103 R. Chemnitzer, G. Auffermann, D. M. Többens and R. Kniep., (Sr_2N) H: Untersuchungen zur Redox-Intercalation von Wasserstoff in Sr_2N, *Z. Anorg. Allg. Chem.*, 2005, **631**(10), 1813–1817, DOI: **10.1002/zaac.200500105**.

104 A. J. E. Rowberg and C. G. Van de Walle, Hydride conductivity in nitride hydrides, *ACS Appl. Energy Mater.*, 2021, **4**(6), 6348–6355, DOI: **10.1021/acsaem.1c01208**.

105 R. Leveque, M. Zanne, D. Vergnat-Grandjean and J.-F. Brice, Etude de la conducivité ionique des hydrurofluorures $CaF_{2-x}H_x$, *J. Solid State Chem.*, 1980, **33**(2), 233–243, DOI: **10.1016/0022-4596(80)90124-3**.

106 M. Kamata, M. Atsushi and E. Takao, Synthesis and Ionic Conductivity of $LiBaF_{3-x}H_x$, *Denki Kagaku Oyobi Kogyo Butsuri Kagaku*, 1998, **66**(4), 443–445, DOI: **10.5796/kogyobutsurikagaku.66.443**.